Available online at www.sciencedirect.com

ScienceDirect

Underground Space 27 (2026) 340–361

www.keaipublishing.com/undsp

Research Paper

Global flow behaviors of multiple shafts in shallow-buried urban road tunnels subjected to fire load

Daolong Xiong, Shiqi Zhang, Yan Ouyang, Yan Tong *, Zelin Liu, Kaiquan Chen, Peng Wang, Yinqing Zhou

College of Urban Construction, Nanjing Tech University, Nanjing 211816, China

Received 9 July 2025; received in revised form 24 September 2025; accepted 29 October 2025
Available online 10 February 2026

Abstract

Shallow-buried urban road tunnels with shafts (URTS) have reduced traffic congestion in large cities. During fire scenarios, the backflows occur at those shafts far away from the fire source inhibiting smoke exhaust, but its rules have been unknown. A 400 m (length) × 12 m (width) × 5.5 m (height) physical model with 6–7 shafts over the ceiling is established using fire dynamic simulator software. The simulations are carried out after validation by both a small-scale experiment and a full-scale experiment. A total of 16 cases with 4 heat release rates (HRRs) and 4 spacing of fire source from the nearest unit shaft #1-1 ($s_{\text{f-us1}}$), are designed. Results indicate that the smoke spreading length is nearly independent of HRR but increases with $s_{\text{f-us1}}$. Ceiling smoke temperatures follow the power exponential laws, and the attenuation coefficients decrease with the increase of HRR and $s_{\text{f-us1}}$. The farther away from the fire, the more likely the occurrence of shaft backflow. A good power exponential rule of the shaft negative mass flow rate is fitted out, and values of decay coefficient b_2 range from 0.56 to 1.0. Based on dimensional analysis, a power exponential rule of the shaft dimensionless net mass flow rate is fitted for the exhaust shafts and a linear rule for the backflow shafts. The shaft neutral plane heights range from 1.4 m to 3.6 m for the exhaust shafts and 3.2 m to 5.4 m for the backflow shafts. Also, a linear rule is fitted. This study establishes the smoke backflow theory in URTS during fire scenarios and contributes to the tunnel fire protection engineering.

Keywords: Tunnel; Shaft; Fire; Smoke; Backflow; Neutral plane

1 Introduction

Urbanization stimulates the wide utilization of underground space for fast transportation, especially in large cities around the world. As one type of urban underground expressways, shallow-buried urban road tunnels with shafts (URTS) have been built and operated, which have successfully reduced the traffic congestion. Examples are the tunnel clusters of the Expressway Inner Ring Line in Nanjing, China (e.g., Xi'an Gate Tunnel, Tongji Gate Tunnel, Mofan Road Tunnel) (Tong et al., 2014), Beidi Road Tunnel in Shanghai, China (Guo et al., 2020), and Chiba section of the Outer Ring Road in Tokyo, Japan (Tanaka et al., 2021). Central green belts are often situated along the median of two-way streets, positioned directly above the junction points between the tunnel's two unidirectional holes. This positioning allows for the construction of vertical shaft groups over the tunnel ceilings, with their top openings situated in the green belts. These shafts are designed to take advantage of thermal buoyancy (hot vehicle emissions during normal operation or hot smoke in fire scenarios) to achieve natural ventilation. It has great advantages of construction cost reduction with low tunnel height, and energy saving without ventilators. Nowadays, tunnel fire safety has already become one of the key issues for any tunnel project, and smoke control is a key issue for

* Corresponding author.
E-mail address: njtongyan@njtech.edu.cn (Y. Tong).
Peer review under the responsibility of Tongji University

https://doi.org/10.1016/j.undsp.2025.10.010

Nomenclature

c_p	air specific heat capacity, kJ/kg·K
D	diameter of the burning area, m
D^*	characteristic fire diameter, m
G	mass flow rate, kg/s
G^*	dimensionless mass flow rate
g	gravity acceleration, 9.8 m/s^2
H	height, m
H_n	neutral plane height of shaft, m
k	opening area ratio of shafts, %
L	length dimension
l	length, m
M	mass dimension
Greek	
ρ	density, kg/m^3
π	dimensionless parameter
Subscripts	
a	ambient
max	maximum
neg	negative
n_1	number of all shafts
n_2	number of all unit shafts per shaft
Q	heat release rate of fire source, kW
Q^*	dimensionless heat release rate of fire source
S^*	dimensionless spacing of fire from the nearest shaft
s	spacing, m
$s_{f\text{-}us1}$	spacing of fire source from the nearest shaft, m
sh	shaft
T	temperature, K
T	temperature dimension
t	time dimension
tu	tunnel
w	width, m
x	distance away from the fire source, m
δx	nominal size of a mesh cell, m

the use of natural shafts in case of a fire (Li & Ingason, 2018).

The development of buoyancy-driven flow in a tunnel can be described in four stages, and a final one- dimensional smoke spreading under the ceiling is the main stage. Tanaka et al. (2021) clarified that the smoke spread length was decided by a balance between the inertia and buoyancy of the hot smoke flow and the inertia of the fresh cold air flow induced by the fire. Zhu et al. (2025) deduced a simple mode to estimate the maximum propagation length for a tunnel with mechanically ventilated shafts. Currently, the ceiling temperature distribution has often been utilized to evaluate smoke spreading in the longitudinal direction of tunnels, mostly those without top openings (Cheng et al., 2022; Gao et al., 2021; Gong et al., 2016; Hu et al., 2005, 2010; Liu et al., 2023; Qiu et al., 2021; Shi et al., 2021; Yang et al., 2020; Zhong et al., 2016). Regardless of T-shaped tunnel and curved tunnel groups (Cheng et al., 2022), or sloped tunnel (Yang et al., 2020), or tunnel with longitudinal ventilation (Gong et al., 2016; Hu et al., 2005, 2010; Shi et al., 2021), a rule of exponential decay has always been fitted. Especially, Hu et al. (2005, 2010) developed a predictive model based on the results of full-scale experiments, and found a power of exponential decay under different longitudinal ventilation speeds. Gong et al. (2016) established a heat balance equation considering the thermal radiation, air entrainment, and heat convection, and derived a dual power-law exponential attenuation equation. Regarding URTS, the ceiling temperature distributions have their own special rules due to the presence of multiple shafts. Rarely, in a series of full-scale firing experiments on two real URTS (Yan et al., 2009; Zhang et al., 2024; Zhou et al., 2025), the powers of the exponential function were consistently drawn even under different ambient temperatures, fire-shaft distances, and whether the shaft axial fan was in operation. Additionally, the determination of decay coefficients was significantly affected by these factors.

Smoke flow modes in tunnel fires can be highly complex. Under certain conditions, smoke propagation may be hindered and transformed into another pattern, resulting in backflow. Currently, most studies have focused on the smoke backflow in longitude under the tunnel ceiling (Ding et al., 2024; Fan et al., 2017; Ying et al., 2025; Zhang et al., 2021; Zhao et al., 2024). For example, Fan et al. (2017) investigated a mine laneway fire and revealed that increasing the vertical height of an inclined laneway decreases the backflow length and that a non-dimensional Richardson number Ri (ratio of the vertical buoyancy force causing the stack effect to the horizontal inertia force generated by the fire source) can distinguish the existence of backflow. Ying et al. (2025) investigated an underground interconnected tunnel and found that a higher heat release rate (HRR) results in a larger backflow; they also developed a predictive model for smoke back layering for an individually ventilated branch tunnel. Zhu et al. (2025) revealed that an increase in either length or angle of an inclined laneway would contribute to the decrease in backflow length in a horizontal laneway, which would lead to more smoke flowing into the inclined laneway. Regarding the tunnel shaft, phenomena such as plug-holing and boundary-layer separation have often been

associated with a single shaft with a large cross-sectional area, which have gained considerable attention (Cong et al., 2017, 2020; Ji et al., 2012, 2013b; Mao & Yang, 2016; Tanaka et al., 2015). Ji et al. (2012) proposed a modified number *Ri'* to determine the flow field inside the shaft, with a critical value of 1.4 for plug-holing occurrence. In practice (Yan et al., 2009; Zhang et al., 2024; Zhou et al., 2025), neither plug-holing nor boundary-layer separation was observed due to each shaft being divided into several small unit shafts, but the evident smoke backflows occurred at the bottom of those shafts, farther away from the fire source. It destroyed the structure of the upper smoke layer and hindered the smoke discharge out of the shafts. Also, Zhang et al. (2024) calculated the number *Ri'* for different shafts and found it to be too large for those farther shafts due to the small horizontal inertia forces arriving at it. Nowadays, the issue of shaft backflow has not been paid much attention. Rarely, Yao et al. (2019) noticed the second pair of shafts' downdraught (backflow), where the smoke front stabilized at its bottom, and explained that the buoyancy force could be too low to overcome the kinetic pressure of the airflow flowing into this shaft.

Mass flow rate of the shaft is often used to quantify the exhaust ability. In fire scenarios, it is necessary to balance the buoyancy and inertial force of the smoke to achieve effective smoke exhaust. Chow and Gao (2011) focused on the competition between buoyancy and inertial forces, and identified the negative pressure zone near vents as a region where pressure-driven flow (inertial) interacts with buoyancy. Guo et al. (2021) estimated the total mass flow rate exhausted from the shaft (both smoke and entrained air) and revealed that the shaft height has a limited contribution to the mass flow rate of the incoming smoke exhausted, but a larger shaft cross-sectional area has a favorable performance in exhausting the smoke. Wang et al. (2023) confirmed that the total mass flow rates decrease with the increase of the length–width ratio of the ceiling vent and that the smoke mass flow rate exhausted by the shaft gradually increases with HRR. Liang et al. (2025) found that the unpowered ventilation caps could improve smoke exhaust efficiency, doubling the mass flow rate, which increases with higher lateral wind speeds.

The neutral plane is characterized by a critical height to distinguish inflow and outflow, where the static pressure difference is zero. The essence of the fire plume is the orifice flow caused by the pressure difference between the inside and outside of the compartment. The higher the opening above the neutral plane, the stronger the thermal buoyancy. The neutral plane height (NPH) is a good index to assess the openings' exhaust ability inside a confined space. Researchers have investigated the distributions of the neutral plane in various fire scenarios, such as high-rise buildings (Li et al., 2014; Yang et al., 2013) and sloping tunnels (Chow et al., 2016; Gao et al., 2022; Shao et al., 2024). Yang et al. (2013) revealed that both the mass inflow rate and the neutral plane location increase as the shaft opening area, shaft height, and expelling gas temperature increase. Li et al. (2014) investigated a 12-storey stairwell with three vents and used the temperature and velocity profiles at the middle opening to determine the location of the neutral plane, which was mainly affected by the middle opening height but weakly by the HRR. Chow et al. (2016) found that the neutral plane of the low tunnel entrance faded away when the longitudinal slope was greater than 9°. Gao et al. (2022) found that NPH at the low entrance of the tunnel increased gradually as the slope increased. Shao et al. (2024) found that the nearer the fire source location is to the low entrance and the greater the slope, the higher the neutral plane position at the high entrance of the tunnel will be.

Methods used in the study of deterministic law of fire science are commonly experimental and numerical calculations. Fire experiments are often hard to conduct due to high cost, structural destructiveness, and human safety, but the data generated are more valuable and credible. Full-scale experiments on tunnel fires have been rarely carried out, especially on URTS (Cheng et al., 2022; Guo et al., 2020; Qiu et al., 2021; Shi et al., 2021; Yan et al., 2009; Yang et al., 2020; Zhang et al., 2024; Zhou et al., 2025). Numerical simulation has been widely used to grasp the smoke flow characteristics, due to good repeatability, time saving, and lower investment cost. Fire dynamic simulator (FDS) is a three-dimensional numerical simulation tool developed by the National Institute of Standards and Technology, Gaithersburg, USA. Current simulations have shown that large eddy simulation (LES) technology in adopting FDS is much reliable in modeling the spread of tunnel fire smoke (Chow et al., 2016; Cong et al., 2017, 2020; Ding et al., 2024; Fan et al., 2017; Gao et al., 2021, 2022; Guo et al., 2021; Hu et al., 2005; Ji et al., 2012, 2013a; Mao & Yang, 2016; Shao et al., 2024; Wang et al., 2023; Yao et al., 2019; Zhang et al., 2021).

From previous researches on fire accidents, the following conclusions can be drawn: (1) URTS feature multiple one-sided shafts with non-uniform spacing, and the smoke spreading under the ceiling is largely influenced by the shaft arrangements and HRRs, but the rules remain unclear; (2) backflows at the shaft bottoms are undesirable because they inhibit smoke discharge, and its characteristics have been rarely addressed; (3) NPHs have been investigated on only one narrow high space, such as a high-rise building or a sloping tunnel. As for multiple shafts in one URTS, understanding its distributions can quantify the global shaft smoke flows, but they also remain unknown.

In this study, a tunnel model with a dimension of 400 m (length) × 12 m (width) × 5.5 m (height) is established, and multiple shafts are arranged over the ceiling with each unit shaft at 3.0 m (length) × 3.0 m (width) × 6.5 m (height). A 1/16 small-scale firing experiment was carried out to observe the exhaust and backflow phenomena. LES are conducted under different HRRs and fire-shaft spacing. Smoke fronts and ceiling smoke temperature attenuation

are determined. Velocities of smoke exhaust or backflow of all unit shafts are obtained and compared, and the mass flow rates are fitted out based on dimensional analysis. The NPHs of all unit shafts are determined, and their relationships with the corresponding mass flow rate are established. This study enriches a theory in the field of URTS firing and contributes to the fire safety regulations of URTS.

2 URTS sizes and a real fire accident

All shafts of each hole must be constructed along one side of the wall so that their tops are located within the green belt, and their widths are perpendicular to the length of the belt. Every shaft has a limited height due to the tunnel's shallow-buried depth and a limited width constrained by the narrow green belt. Consequently, the shaft length is the only flexible structural parameter. There is a note that every shaft is evenly separated by several beams to solidify the tunnel structure, which has a fixed size of 0.8 m in thickness with its bottom paralleling to the shaft bottom opening. Table 1 lists the dimensions of six URTS in Nanjing, China. It is known that all holes are nearly identical in width (about 12.0 m) and height (about 6.0 m), but some differ in length (1136–1720 m). All shafts are in the range of 1.1 to 11.0 m in height (mostly around 5.0 m), and 2.6 to 3.0 m in width, but differ largely in length, ranging from 6.2 to 22.4 m. The solid beams separate each shaft evenly into 2 to 7 unit shafts with each having a fixed length of around 3.0 m. The spacing between two adjacent shafts differs largely among tunnels or even in one tunnel. Especially, when the tunnel crosses under a street intersection or a water body, there is no space to build a green belt on the streets, then a long shaft spacing is created (e.g., in Xi'an Gate Tunnel at 240 m). The number of shafts was 10 to 24 for all six URTS.

A shaft spacing, s (m), is defined as the distance between two adjacent shafts. Assuming the shafts are evenly spaced, it can be determined according to Eq. (1):

$$s = \frac{l_{tu}}{n_1} - l_{sh} \times n_2, \tag{1}$$

where l_{tu} is the tunnel length, m; l_{sh} is the unit shaft length, m; n_1 is the number of all shafts; n_2 is the number of all unit shafts per shaft. A shaft opening area ratio k (%) is defined as the area ratio of all shafts' top openings to the tunnel's horizontal projection. It can be calculated based on Eq. (2):

$$k = \frac{100 \times l_{sh} \times w_{sh} \times n_1 \times n_2}{l_{tu} \times w_{tu}}, \tag{2}$$

where w_{tu} is the tunnel width, m; w_{sh} is the unit shaft width, m. In real scenarios, values of k are in the range of 2.78% to 3.86%, as seen in Table 1. As an example of one URTS having a size of 800 m (length) × 12 m (width) with uniform shaft spacing, also each unit shaft having a size of 3.0 m (length) × 3.0 m (width), relationships among parameters of n_1, n_2, s, and k are determined respectively based on Eqs. (1) and (2). The results are given in Fig. 1. Values of s change in a large range of 40 to 260 m, and decrease with the increase of n_2 or n_1, but the decreasing tendencies are basically identical in spite of n_1. Values of k change in the range of 0.5% to 10% and increase with the increase of n_2 or n_1. The larger the n_1, the more rapid the increase in k. The smaller the n_2, the less the differences in k among n_1.

A real fire accident occurred on February 27, 2023, in the westbound of Xi'an Gate Tunnel in Nanjing, China, and the entire process was captured on video. As shown in Fig. 2, the westbound consists of three lanes. The shafts were installed over the ceiling along the left side wall, with some spacing between them. A minibus caught fire in the right lane, very close to one of the shafts. Just after ignition, the smoke was minimal, and visibility was good, as depicted in Fig. 2(a). However, 600 s after ignition, the flames intensified, causing severe traffic congestion. A large amount of smoke spread and reached the bottom of the nearest shaft, but the visibility was still good due to the smoke accumulation just under the ceiling, as seen in Fig. 2(b). Overall, the one-sided shafts play an important role in fire smoke exhaust.

3 Small-scale model experiments

3.1 Experimental design

In fire scenarios, the relationship between a scaled model and a prototype is mostly described by Froude's scaling law. On this basis, the following equations are obtained:

Table 1
Sizes of six URTS in Nanjing, China.

Tunnel	Hole ($L \times W \times H$) (m × m × m)	Shaft				Opening area ratio, k (%)
		Size ($L \times W \times H$) (m × m × m)	Number	Spacing (m)	Beam number/shaft	
Mofan Road	1136 × 12.5 × 5.7	8.8 × 3.0 × (1.1–4.5)	15	41–177	1	2.78
Xi'an Gate	1720 × 12.0 × 6.0	12.8 × 2.6 × (4.9–7.8)	24	24–240	3	3.86
Tongji Gate	1340 × 10.5 × 6.0	12.8 × 2.6 × (6.0–7.6)	14	23–116	3	3.31
Shuixi Gate	1280 × 11.5 × 6.0	(6.2–22.4) × 3.0 × (4.2–11.0)	10	10–275	1–6	2.93
Qingliang Gate	1655 × 11.5 × 6.0	(13.6–20.4) × 3.0 × (1.8–4.8)	14	26–233	3–5	3.06
Wutang	1590 × 11.8 × 6.0	9.9 × 3.0 × (4.1–9.2)	21	40–120	2	3.32

$$\frac{Q_m}{Q_f} = \gamma^{5/2}, \tag{3}$$

$$T_p = T_m, \tag{4}$$

$$\frac{\tau_m}{\tau_p} = \gamma^{1/2}, \tag{5}$$

where Q is the fire HRR, kW; T is the temperature, K; τ is the time, s; γ is the size scale ratio of the model to the prototype. The subscripts m and p represent the model and the prototype, respectively. The results of the experiment using a scale-model tunnel fire can correspond to those of a full-scale tunnel fire. A pool fire's HRR Q is proposed as follows (Babrauskas, 1983):

$$Q = xm'\left(1 - e^{-k\beta D}\right)A_f\Delta H_c, \tag{6}$$

where x is the combustion efficiency, %; m' is the maximum mass loss rate, g/(s·m^2); $k\beta$ is the empirical constant, m^{-1}; D is the diameter of the burning area, m; A_f is the horizontal burning area, m^2; ΔH_c is the combustion heat, MJ/g. In this study, methanol was used as the fire source, which burns with a flame that is hardly visible, indicating that very little soot is produced. For methanol (Karlsson & Quintiere, 2000), x closes to unity, m' is 17.0 g/(s·m^2), ΔH_c is 0.02 MJ/g for a large pool (pool diameter >0.2 m), and $k\beta$ is independent of the pool diameter. Furthermore, Anghel et al. (2017) advised the $k\beta$ to be 100 m^{-1} for methanol.

Based on the real tunnel size, a 1/16 small-scale model tunnel was built. It has a size of 23 m (length) × 0.75 m (width) × 0.36 m (height), and includes 2 firing segments and 7 non-firing segments, each having a length of 2.5 m. The firing segments are made of 304 stainless steel, and each of them has a tempered glass window on the front side wall for observation. The non-firing segments are made of 10-mm-thick fireproof board, except for the fireproof-acrylic front side wall used for observation. A total of three nonfiring segments are arranged on the left side of the firing segments, and four are on the right. A total of two

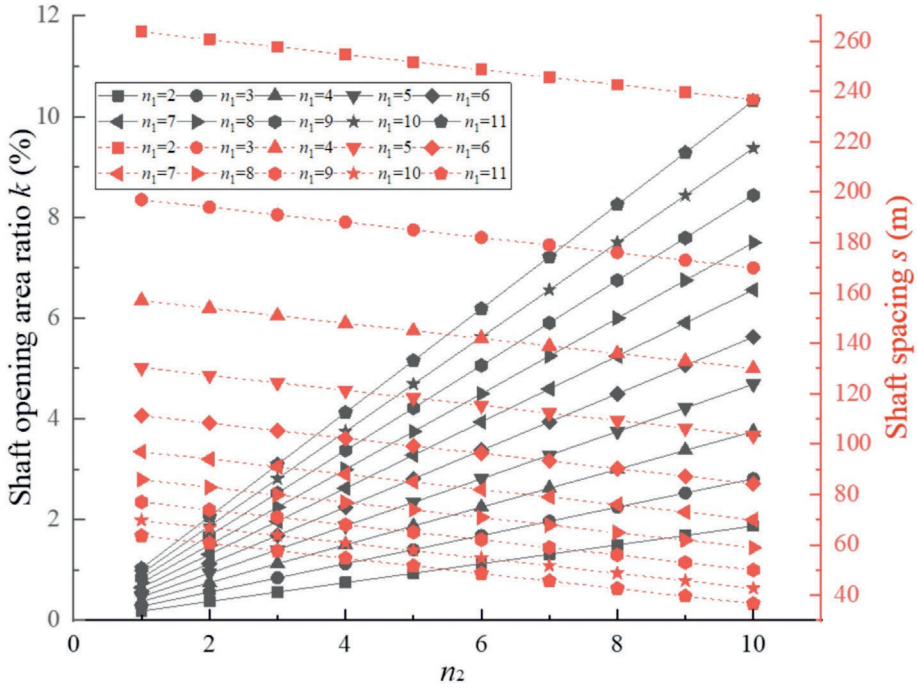

Fig. 1. Relationships among shaft sizes in an 800 m long URTS.

(a) (b)

Fig. 2. Scenarios of a real fire accident in Xi'an Gate Tunnel on February 27, 2023. (a) t = 0 s, and (b) t = 600 s.

fireproof-acrylic shafts are installed uniformly over the ceiling along the back side wall of each nonfiring segment, and each shaft has a size of 0.8 m (length) × 0.2 m (width) × 0.3 m (height). Three equally spaced grooves are excavated along the inner wall of the shaft in the longitudinal direction. Three vertical partition plates can be respectively inserted into these grooves, thereby dividing the shaft into four unit shafts. A horizontal partition plate is used to cover the bottom of any one of the unit shafts, making the number of unit shafts participating in smoke exhaust adjustable. Additionally, the spacing between two adjacent shafts is adjustable. The scenes of the small-scale model tunnel are depicted in Fig. 3.

In this study, after some shaft top openings were sealed with horizontal partition plates, each shaft was left with only 3 unit shafts, and the spacing of the fire source away from the nearest unit shaft ($s_{\text{f-us1}}$) was finally 7.7 m (equivalent to 122 m in the prototype). A 304 stainless steel rectangular pan was centrally placed on the firing-segment ground with methanol used as the fire source. The mass loss rates were measured in real time with burning areas by a WT-B electric balance (accuracy of 0.01 g). A rate of 15.18 g/(s·m^2) was obtained for a burning area of 0.08 m (width) × 0.14 m (length). Based on Eq. (6), a fire power of 3.64 kW was determined, which corresponds to a fire power of 5 MW in the prototype according to the scaling law. Smoke cakes were added above the pan to increase the amount of smoke in the fire. A series of TT-K-30-SLE (K type) thermocouple trees were placed in longitude within 7.7 m from the fire source, and the ceiling temperatures were recorded by a data-acquisition instrument with three channel modules. The ambient air temperature was 18.0 °C. An EP532-200 laser sheet (with a 1.2 MW output power) was placed at the tunnel's left entrance to facilitate visualization. A camera was used to record the smoke spreading phenomena.

3.2 Smoke spreading phenomena

Figure 4 presents the scenes of flame and smoke spreading in the model-scale experiment. The geometry of a turbulent diffusion flame is dominated by the turbulent mixing between the gaseous fuel and the entrained air (Jiao et al., 2025). Especially, in naturally ventilated tunnels, the flame height is dominated by HRR (He et al., 2021; Yuan et al., 2024). As seen in Fig. 4(a), the flame rose up directly but didn't hit the ceiling. In the buried section before the smoke arrived at the nearest shaft #1, as seen

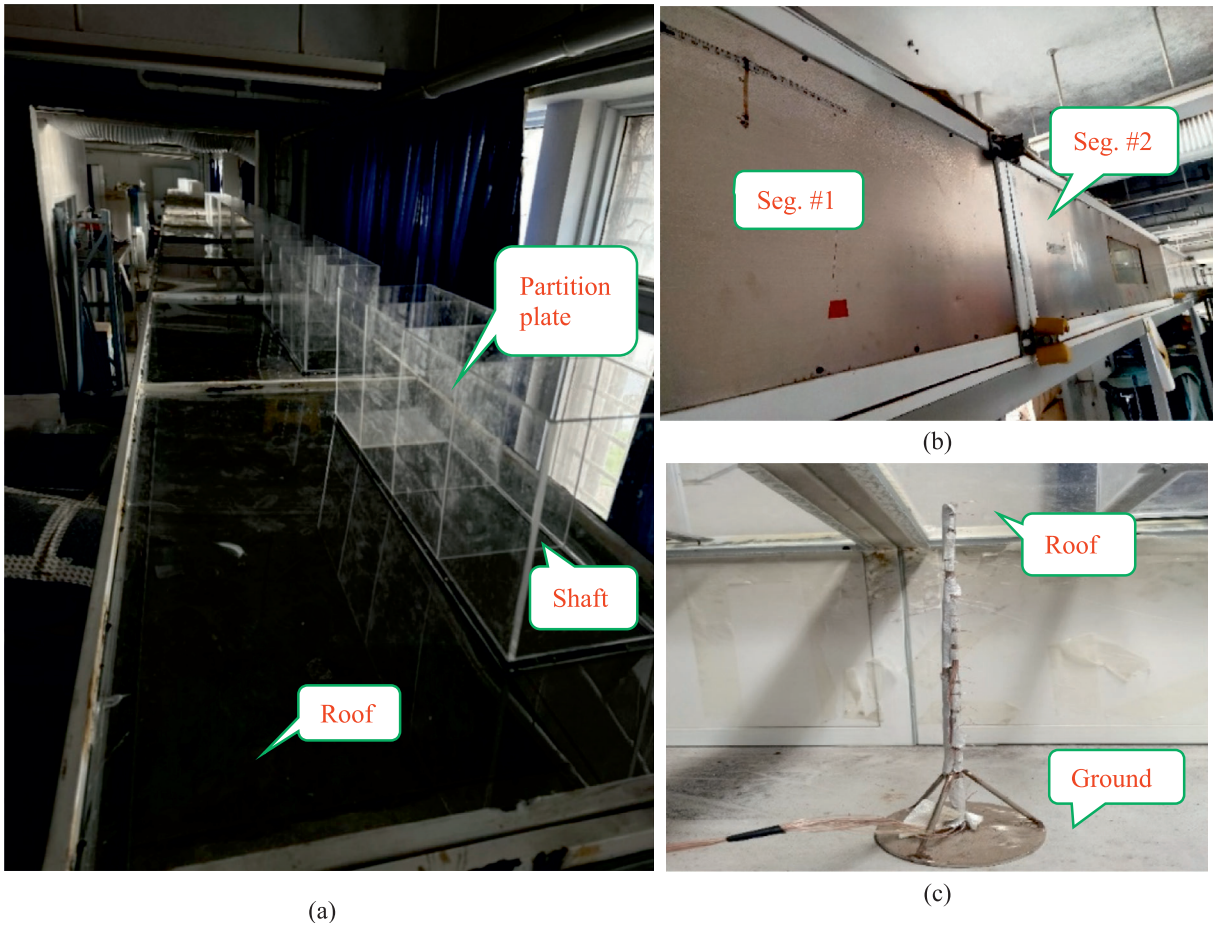

Fig. 3. Scenes of the small-scale model tunnel. (a) The whole tunnel, (b) two firing segments, and (c) a thermocouple tree inside the tunnel.

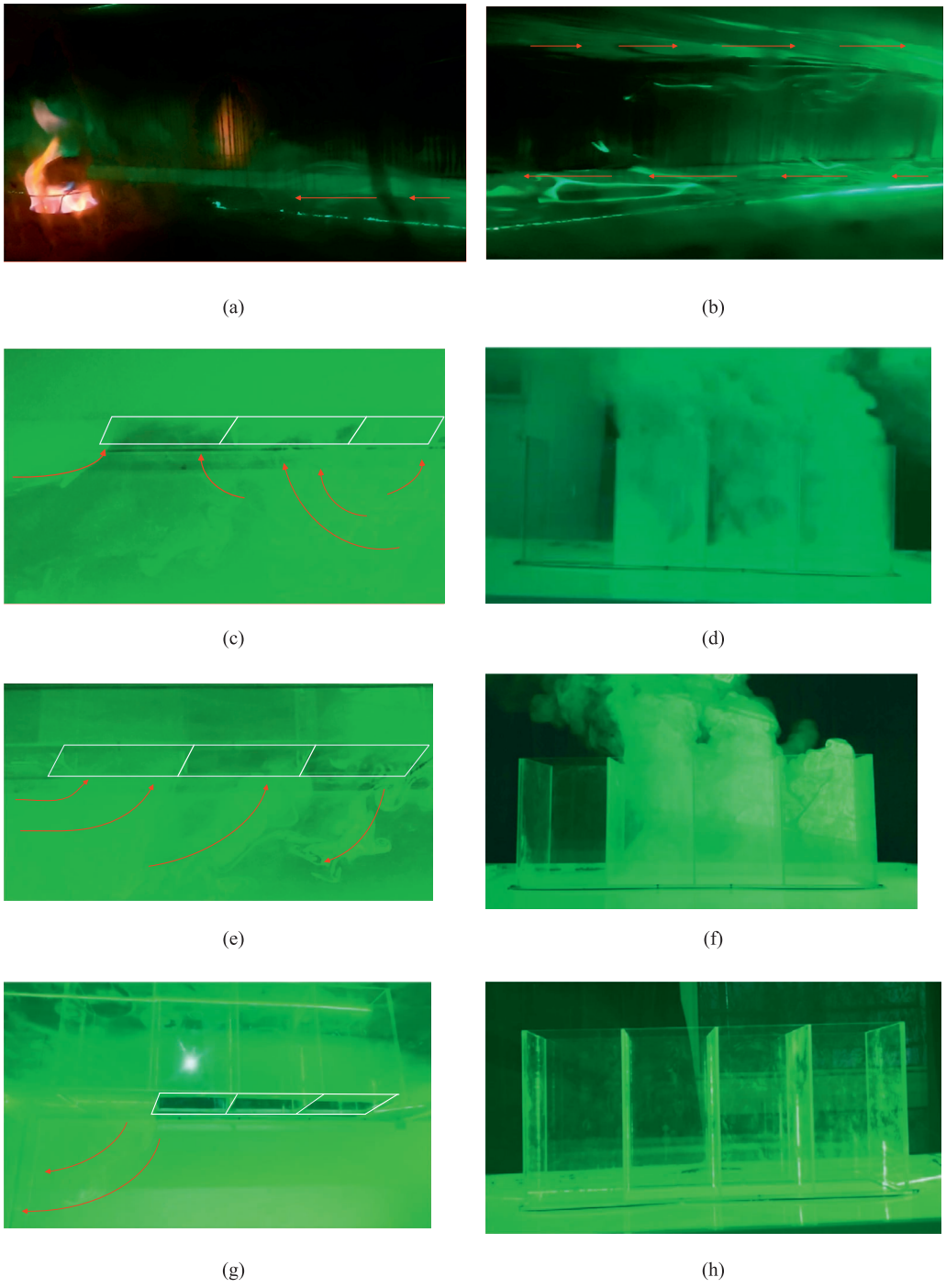

Fig. 4. Smoke spreading under HRR = 3.64 kW and $s_{f\text{-}us1}$ = 7.7 m in the small-scale experiment. (a) Fire source in burning, (b) before arriving at shaft #1, (c) at the bottom of shaft #1, (d) inside and outside shaft #1, (e) at the bottom of shaft #2, (f) inside and outside shaft #2, (g) at the bottom of shaft #3, and (h) inside and outside shaft #3.

in Fig. 4(b), an evident stratification existed between layers of the upper and the lower sections where an upper hot smoke spreads towards the entrance, but a reversal flow existed at the tunnel bottom. As seen in Fig. 4(c) and (d), shaft #1 played an important role in exhausting, and the turbulences occurred extensively at the shaft bottom and inside the shaft; also, there were nearly no plug-holing or boundary separation. As seen in Fig. 4(e) and (f), shaft #2 is far away from the fire source, and only unit shafts #2-1 and #2-2 had an exhaust phenomenon, but unit shaft #2-3 had a backflow phenomenon. As seen in Fig. 4(g) and (h), the smoke front could not arrive at shaft #3 (farther away from the fire source), and no smoke was found at the shaft bottom and inside the shaft. Furthermore, the measured maximum ceiling temperature rises are depicted in Fig. 5, where the distance is converted to the prototype

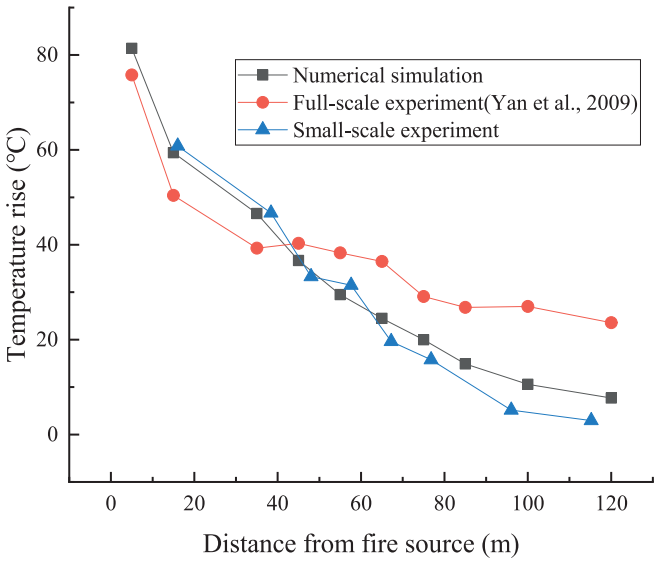

Fig. 5. Comparisons of the maximum ceiling temperatures between the experiments and FDS simulation.

length. It is known that the temperature rises decayed rapidly away from the fire source, reaching up to 60 °C at about 13 m, and tended to be ambient at about 120 m.

A schematic view of global smoke flow behaviors during firing scenarios is depicted in Fig. 6. A large amount of hot smoke is released from the fire source, spreads under the ceiling, and is possible to exhaust out of the nearest shaft driven by a strong thermal buoyancy. As the smoke travels, thermal buoyancy is weakened due to the heat loss. However, due to the oxygen consumption by combustion, a negative pressure effect is created around the fire source. So, the airflows tend to be induced towards the fire source, which comes from the tunnel openings, including the two entrances and the shaft top openings. Once the smoke thermal buoyancy is less than the inertial force of the induced airflow, the smoke will be suppressed and even flow in the opposite direction. The complex reversal flows would occur simultaneously in the driving zone and inside the shafts. Also, backflow behaviors may differ among shafts, which are dependent on some factors, such as HRR, shaft size, and shaft spacing.

4 Numerical methods

Complementary computational fluid dynamic (CFD) simulations are carried out by adopting FDS version 4.0.7. An approximate form of Navier–Stokes equations appropriate for low Mach number applications is used. To handle subgrid-scale convective motion, LES technique is adopted, and the smallest eddies are filtered out of the governing equations.

4.1 Model settings

A physical model at 400 m (length) × 12 m (width) × 5.5 m (height) is established in FDS. Several one-sided shafts are built over the ceiling with each having a fixed size of 3.0 m (width) × 6.0 m (height). Two beams separate each shaft into three even unit shafts in longitude, and each unit shaft has a length of 3.0 m. The spacing is adjustable between shaft #1 and the tunnel's left entrance but fixed to be 41.0 m between any two adjacent shafts. During firing, extensive heat and mass transfer would exist between the inside and outside sections. A 320.0 m (length) × 5.0 m (width) × 7.6 m (height) virtual domain is extended over the shaft top openings with its bottom being parallel to the shaft top openings. A 10.0 m (length) × 14.0 m (width) × 8.6 m (height) virtual domain is extended, which is adjacent to the tunnel's right entrance with its bottom on the ground. The physical model established in FDS and its schematic views are depicted in Fig. 7. FDS (McGrattan et al., 2014) provides a vent with SURF_ID= "MIRROR" that is of no-flux and free-slip. With the mirror acting, an entire face of the computational domain is spanned, essentially doubling the size of the domain as a plane of symmetry. From the point view of enough computational domain and fewer CPU resources, the tunnel left entrance is set to be a mirror vent.

A square pool fire is placed at the center line of the tunnel on the ground, and its left side is just parallel to the tunnel's left entrance. A steady HRR per unit area (HRRPUA) is adopted to be 1250 kW/m^2. The tunnel's right entrance is set to be an open boundary, including all surfaces of two extended virtual domains adjacent to

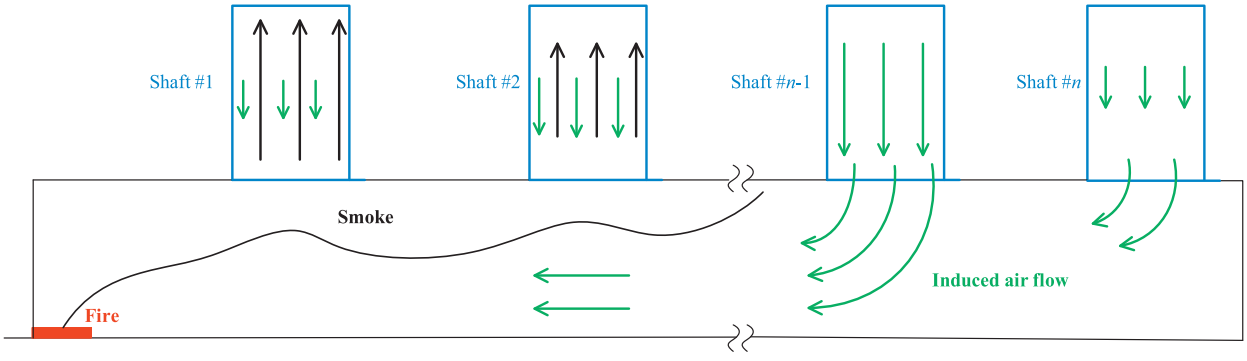

Fig. 6. Schematic view of the smoke spreading and the induced airflows in URTS firing.

the outside. The ground, ceiling, and all walls are specified as "CONCRETE" with a thickness of 0.5 m. The surface heat transfer coefficient is set to 15.59 W/(m^2·K). An ambient temperature of 20 °C with an ambient pressure of 101 325 Pa is adopted, and the simulation time is set to be 600 s.

Monitoring points of temperature are arranged under the ceiling in the driving zone at an interval of 0.5 m in longitude. Monitoring points of velocity are arranged inside each unit shaft. Every three of them are, respectively, at z = 0, 1.0, 2.0, 3.0, 4.0, 5.0, and 6.0 m at an interval of 0.7 m in width. Every seven of them are respectively at x = 0.7, 1.4, and 2.1 m at an interval of 1.0 m in height. Slices of both temperature and velocity are arranged on the plane of y = 1.5 m, that is 1.5 m away from the tunnel front sidewall. FDS (McGrattan et al., 2014) provides "MASS FLOW" to output the net integrated mass flux through the given planar area, oriented in the positive z direction. Also, "MASS FLOW+" or "MASS FLOW–" yields the integral of the flow in the positive or negative direction only. In this study, mass flow rates are measured on the tunnel right entrance and all shaft top openings, and three properties of "positive," "negative," and "both" are adopted on all of them to obtain the inflows and outflows. The monitoring point arrangements are shown in Fig. 7.

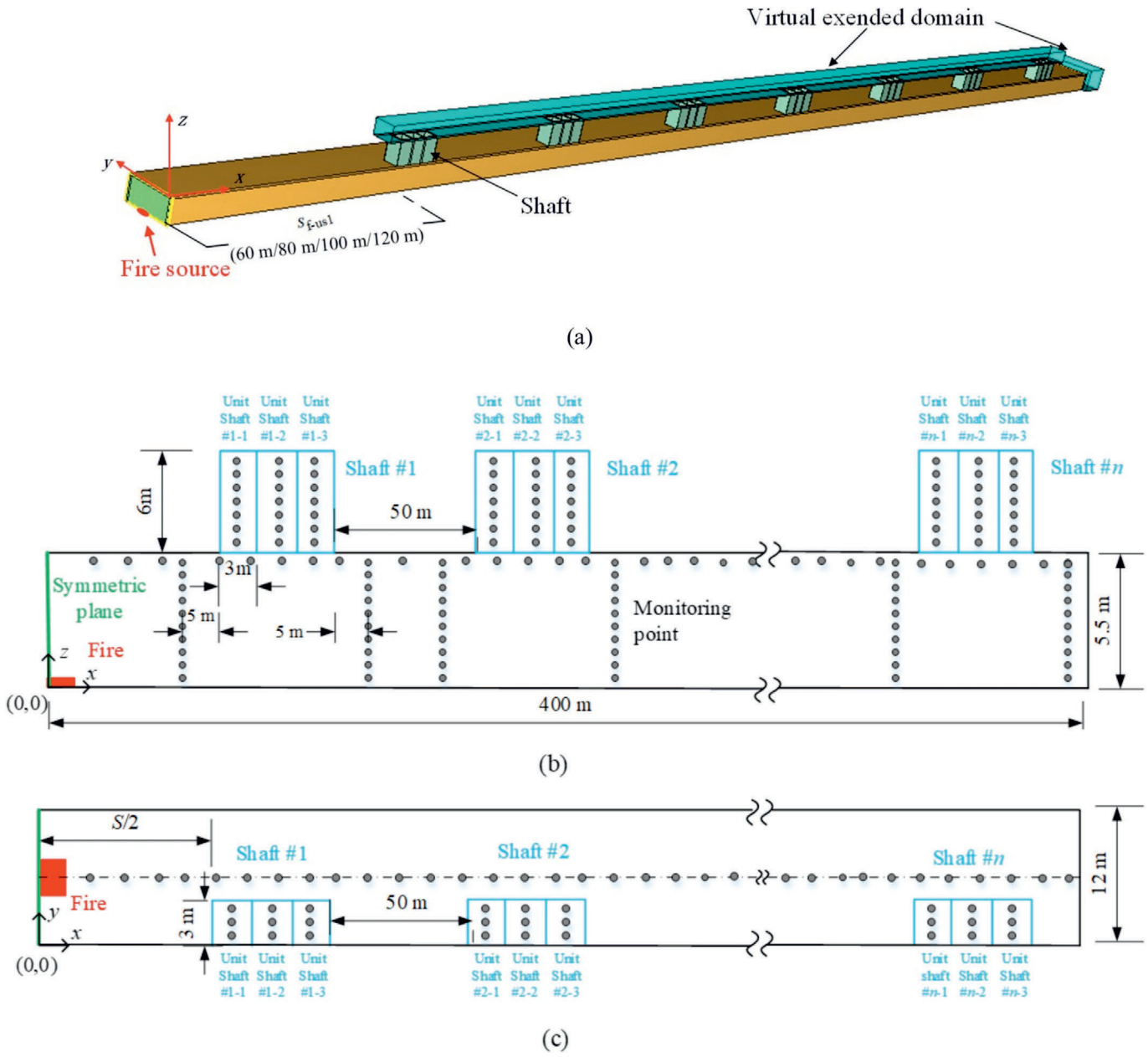

Fig. 7. Schematic views of the physical model and monitoring points in simulations. (a) Physical model established in FDS, (b) front view, and (c) top view.

4.2 Grid sensitivities

Intensive heat and mass transfer would occur around the fire source, and the flows inside the shafts are required to be known in detail. Then, a multi-mesh system is established, which includes 1 firing domain with a size of 16 m (length) × 12 m (width) × 5.5 m (height), covering the fire source, 6–7 shaft domains (one shaft, one domain), 2 virtual extended domains, and 1 non-firing domain in the driving zone. Adjacent domains are just beside each other. Grid sizes of the firing domain and all shaft domains are the same, and half of the other domain. The smaller the HRR, the finer the grid, but the longer the CPU operating time. As an example of 5 MW fire source, four mesh sizes of the firing domain are tested, which are 0.2, 0.3, 0.4, and 0.5 m/grid, respectively. Parallel simulations are carried out on an Intel Xeon E5-2696 version 3, 2.30 GHz processor, which has 36 cores and 72 threads. With the decrease of mesh size, the temperatures tend to converge, but the CPU operating times increase rapidly. Finally, the 0.2 m/-grid is adopted on domains of all shafts and the fire source, and the 0.4 m/grid on the other domains.

4.3 Verifications of FDS modelling

In terms of the rationality of the mirror vent, a full-size physical model is established, which has a length of 800 m with two open entrances but without a mirror vent. In the case of HRR = 20 MW and $s_{f\text{-}us1}$ = 60 m, simulations are carried out on models of both the full-size and the half-size with a mirror vent (Fig. 7). The results are compared for temperatures and CO concentrations in longitude under the ceiling and the net mass flow rates of unit shafts, respectively. It is found that little difference exists between them, as illustrated in Fig. 8. Therefore, the "mirror" hypothesis is rational and has no impact on the smoke spreading in the whole tunnel.

A full-scale firing experiment (Yan et al., 2009) is selected for verifying the FDS modelling. It was conducted in the eastbound of Xi'an Gate Tunnel in 2007, and a 1.8 m (length) × 1.8 m (width) diesel oil pan (about 5 MW HRR) was placed on the ground in the middle of the longest 240-m buried section (120 m away from the nearest shaft). A longitudinal ambient wind was steady at about 1.0 m/s, and the ambient temperature was 6 °C. A FDS simulation is carried out with a 5 MW fire source 120 m away from the nearest shaft. The maximum ceiling temperature rises of the full-scale experiment in the downstream, the small-scale experiment, and the simulation are depicted in Fig. 5. It is known that all temperature rises decay away from the fire source, exhibiting a favorable trend. When comparing the simulation and the small-scale experiment, the temperature rises are quite close to each other, especially within a range of 65 m, but the simulation has larger rises once beyond 65 m. The discrepancy can be attributed to the heat lost out of the uninsulated tunnel walls and ground in the small-scale experiment, and the farther away from the fire source, the more the heat loss. So, the deviation increases with the distance from the fire source but remains within 5.4 °C at 100 m. When comparing the simulation and the full-scale experiment, the simulation has smaller rises beyond 45 m. This discrepancy originates from the presence of ambient wind in the full-scale experiment, causing the hot smoke to spread farther and accumulate under the ceiling at greater distances. The deviation increases with distance from the fire source but remains within 16.4 °C at 120 m. Furthermore, the smoke front was observed to arrive at the 210 m downstream in the full-scale experiment (Yan et al., 2009), the 10.1 m (equivalent to 161 m in the prototype) in the small-scale experi-

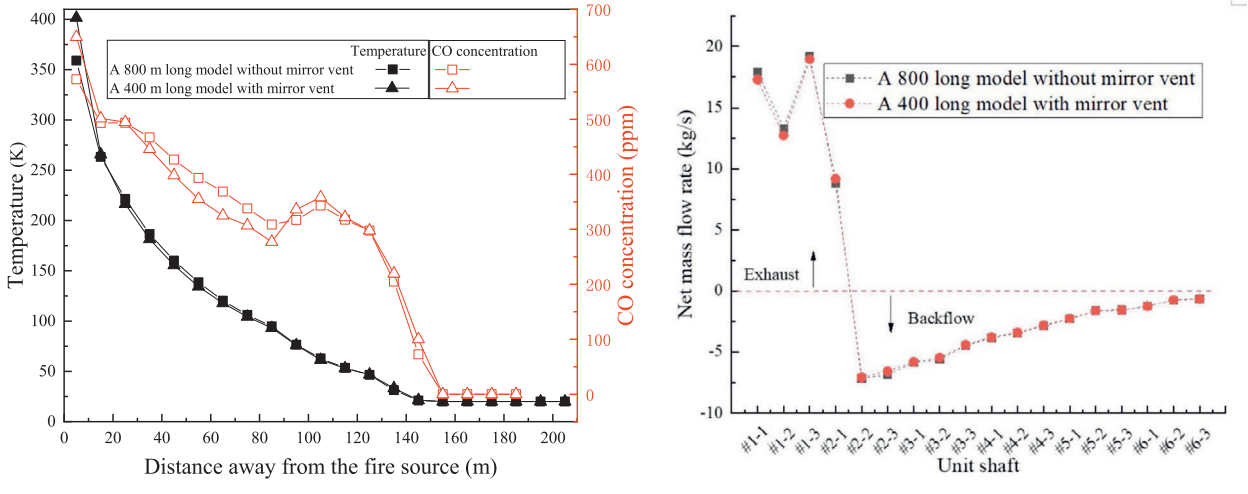

(a) (b)

Fig. 8. Comparisons of simulated results between an 800-m-long model (without mirror vent) and a 400-m-long model (with mirror vent). (a) Temperature and CO concentration, and (b) net mass flow rate of the unit shaft.

ment, and the 170 m in the simulation. Three of them get close to each other. Differences come from two facts: the blurred smoke front and the ambient wind forcing the smoke to spread longer in the full-scale experiment. Overall, the simulation is verified by both the full-scale experiment and the small-scale experiment.

4.4 Modelling cases

When ambient wind or vehicle blockage is not considered, the fire source located at the midpoint of the longest buried section (where the adjacent shafts have the greatest distance) poses the greatest danger, because the smoke has to travel the longest distance to reach the first shaft (unit shaft #1-1) for exhaust. In this study, values of $s_{\text{f-us1}}$ are set at 60, 80, 100, and 120 m based on the tunnel's real size (Table 1). Meanwhile, all other shaft spacing remains constant at 41 m. For the established 400-m-long tunnel, the total number of shafts required is then determined to be 7, 7, 6, and 6, respectively. Consequently, the shaft opening area ratios (k) nearly reach the same values of 3.93% and 3.37% in all cases, based on Eq. (2).

On-site investigations on URTS found that the family's five-seated cars accounted for more than 90%, and the others are vans and buses (Tong et al., 2014). In the field of traditional fuel vehicles, Permanent International Association of Road Congresses (World Road Association, 1999) recommends the design fires for road tunnels that a car fire is in the range of 2.5 to 8 MW, Ingason (1995) gives a van fire at approximately 15 MW and a bus fire at approximately 20 MW, and Soundararajan et al. (2025) revealed that ULDP20G40 (200 mL ULDP + 800 mL Diesel + 40 ppm GQD) exhibited a 6.49% lower maximum HRR compared to raw diesel in a diesel engine. The world is moving towards clean energy in every aspect of the automobile. Bibin et al. (2021) investigated an 8-cell lithium-ion battery pack to determine its thermal behavior and revealed that cell temperature and cell voltage are critical parameters in reducing the internal heat of a battery. In this study, by adjusting the fire source area under the given 1250 kW/m^2 HRRPUA, four steady HRRs of 5, 10, 15, and 20 MW are determined. Finally, a total of 16 cases are designed for simulations as listed in Table 2.

5 Dimensional analysis of the shaft net mass flow rate

Parameters influencing the shaft net mass flow rate are selected, which include HRR, spacing between the fire source and the nearest shaft, spacing between two adjacent shafts, shaft height, ambient air density and temperature, gravitational acceleration, and air-specific heat capacity. These physical parameters, symbols, and dimensions are shown in Table 3.

Consequently, the mass flow rate of the shaft can be expressed as

$$f\left(G_{\text{sh-net}}, Q, T_{\text{a}}, H_{\text{sh}}, s_{\text{sh}}, s_{\text{f-us1}}, \rho_{\text{a}}, c_p, g\right) = 0. \tag{7}$$

M, L, t, and T are selected as the basic dimensions; H_{sh}, ρ_{a}, g, and T_{a} are selected as the basic parameters; the dimensionless equations for the other five parameters can be expressed as follows:

$$\begin{cases} \pi_1 = H_{\text{sh}}^{\alpha_1} g^{\beta_1} \rho_{\text{a}}^{\gamma_1} T_{\text{a}}^{\xi_1} G_{\text{sh-net}} = \text{L}^{\alpha_1} \left(\text{Lt}^{-2}\right)^{\beta_1} \left(\text{ML}^{-3}\right)^{\gamma_1} (\text{T})^{\xi_1} G_{\text{sh-net}}, \\ \pi_2 = H_{\text{sh}}^{\alpha_2} g^{\beta_2} \rho_{\text{a}}^{\gamma_2} T_{\text{a}}^{\xi_2} Q = \text{L}^{\alpha_2} \left(\text{Lt}^{-2}\right)^{\beta_2} \left(\text{ML}^{-3}\right)^{\gamma_2} (\text{T})^{\xi_2} Q, \\ \pi_3 = H_{\text{sh}}^{\alpha_3} g^{\beta_3} \rho_{\text{a}}^{\gamma_3} T_{\text{a}}^{\xi_3} s_{\text{f-us1}} = \text{L}^{\alpha_3} \left(\text{Lt}^{-2}\right)^{\beta_3} \left(\text{ML}^{-3}\right)^{\gamma_3} (\text{T})^{\xi_3} s_{\text{f-us1}}, \\ \pi_4 = H_{\text{sh}}^{\alpha_4} g^{\beta_4} \rho_{\text{a}}^{\gamma_4} T_{\text{a}}^{\xi_4} s_{\text{sh}} = \text{L}^{\alpha_4} \left(\text{Lt}^{-2}\right)^{\beta_4} \left(\text{ML}^{-3}\right)^{\gamma_4} (\text{T})^{\xi_4} s_{\text{sh}}, \\ \pi_5 = H_{\text{sh}}^{\alpha_5} g^{\beta_5} \rho_{\text{a}}^{\gamma_5} T_{\text{a}}^{\xi_5} c_p = \text{L}^{\alpha_5} \left(\text{Lt}^{-2}\right)^{\beta_5} \left(\text{ML}^{-3}\right)^{\gamma_5} (\text{T})^{\xi_5} c_p, \end{cases} \tag{8}$$

Table 2
Cases used for FDS simulation.

Case	Shaft				Fire source		
	Number	Spacing (m)	Unit shaft number	Opening ratio k (%)	Area (m^2)[a]	HRR (MW)[a]	$s_{\text{f-us1}}$ (m)
1–4	7	41	3	3.93	4.0/8.0/12.0/16.0	5/10/15/20	60
5–8	7	41	3	3.93	4.0/8.0/12.0/16.0	5/10/15/20	80
9–12	6	41	3	3.37	4.0/8.0/12.0/16.0	5/10/15/20	100
13–16	6	41	3	3.37	4.0/8.0/12.0/16.0	5/10/15/20	120

[a] An entire face is spanned, doubling the size of the domain by adopting a "mirror" vent.

Table 3
Physical parameters influencing $G_{\text{sh-net}}$.

No.	Physical parameter	Symbol	Dimension	No.	Physical parameter	Symbol	Dimension
1	Heat release rate	Q	ML^{2}t^{-3}	6	Ambient air density	ρ_{a}	ML^{-3}
2	Spacing between fire and nearest shaft	$s_{\text{f-us1}}$	L	7	Ambient air temperature	T_{a}	T
3	Spacing between two adjacent shafts	s_{sh}	L	8	Gravitational acceleration	g	Lt^{-2}
4	Shaft height	H_{sh}	L	9	Air-specific heat capacity	c_p	L^{2}t^{-2}T^{-1}
5	Net mass flow rate of shaft	$G_{\text{sh-net}}$	Mt^{-1}				

where α, β, γ, and ξ are variable coefficients. The indexes of the physical quantities can be solved by the following conservation principle:

$$\begin{cases} \alpha_1 = -5/2,\ \beta_1 = -1/2,\ \gamma_1 = -1,\ \xi_1 = 0, \\ \alpha_2 = -7/2,\ \beta_2 = -3/2,\ \gamma_2 = -1,\ \xi_2 = 0, \\ \alpha_3 = -1,\ \beta_3 = 0,\ \gamma_3 = 0,\ \xi_3 = 0, \\ \alpha_4 = -1,\ \beta_4 = 0,\ \gamma_4 = 0,\ \xi_4 = 0, \\ \alpha_5 = -1,\ \beta_5 = -1,\ \gamma_5 = 0,\ \xi_5 = 1. \end{cases} \tag{9}$$

The dimensionless equations can be simplified as follows:

$$\begin{cases} \pi_1 = \dfrac{G_{\text{sh-net}}}{H_{\text{sh}}^{\frac{5}{2}} g^{\frac{1}{2}} \rho_{\text{a}}}, \\ \pi_2 = \dfrac{Q}{H_{\text{sh}}^{\frac{7}{2}} g^{\frac{3}{2}} \rho_{\text{a}}}, \\ \pi_3 = \dfrac{s_{\text{f-us1}}}{H_{\text{sh}}}, \\ \pi_4 = \dfrac{s_{\text{sh}}}{H_{\text{sh}}}, \\ \pi_5 = \dfrac{c_p T_{\text{a}}}{H_{\text{sh}} g}. \end{cases} \tag{10}$$

According to the relevant criteria of similarity theory, Eq. (7) can be replaced by the following equation:

$$\begin{aligned} & f\left(\frac{G_{\text{sh-net}}}{H_{\text{sh}}^{\frac{5}{2}} g^{\frac{1}{2}} \rho_{\text{a}}}, \frac{Q}{H_{\text{sh}}^{\frac{7}{2}} g^{\frac{3}{2}} \rho_{\text{a}}}, \frac{s_{\text{f-us1}}}{H_{\text{sh}}}, \frac{s_{\text{sh}}}{H_{\text{sh}}}, \frac{c_p T_{\text{a}}}{H_{\text{sh}} g}\right) = 0 \\ \Rightarrow & \frac{G_{\text{sh-net}}}{H_{\text{sh}}^{\frac{5}{2}} g^{\frac{1}{2}} \rho_{\text{a}}} = f\left(\frac{Q}{H_{\text{sh}}^{\frac{5}{2}} g^{\frac{1}{2}} \rho_{\text{a}} c_p T_{\text{a}}}, \frac{s_{\text{f-us1}}}{s_{\text{sh}}}\right) \\ \Rightarrow & \frac{G_{\text{sh-net}}}{H_{\text{sh}}^{\frac{5}{2}} g^{\frac{1}{2}} \rho_{\text{a}}} = f\left(\frac{Q s_{\text{sh}}}{H_{\text{sh}}^{\frac{5}{2}} g^{\frac{1}{2}} \rho_{\text{a}} c_p T_{\text{a}} s_{\text{f-us1}}}\right) \\ \Rightarrow & G^*_{\text{sh-net}} = f\left(\frac{Q^*}{S^*}\right), \end{aligned} \tag{11}$$

where $Q^* = \dfrac{Q}{H_{\text{sh}}^{\frac{5}{2}} g^{\frac{1}{2}} \rho_{\text{a}} c_p T_{\text{a}}}$, $S^* = \dfrac{s_{\text{f-us1}}}{s_{\text{sh}}}$, and $G^*_{\text{sh-net}} = \dfrac{G_{\text{sh-net}}}{H_{\text{sh}}^{\frac{5}{2}} g^{\frac{1}{2}} \rho_{\text{a}}}$.

6 Results and discussions

6.1 Smoke spreading under the ceiling

In all simulations, the flames rise up directly and hit the ceiling when the HRRs are 15 and 20 MW, but do not when the HRRs are 5 and 10 MW. As an example of case 8, Fig. 9 gives views of the flame and the smoke at different times provided by FDS simulations. It is known that the

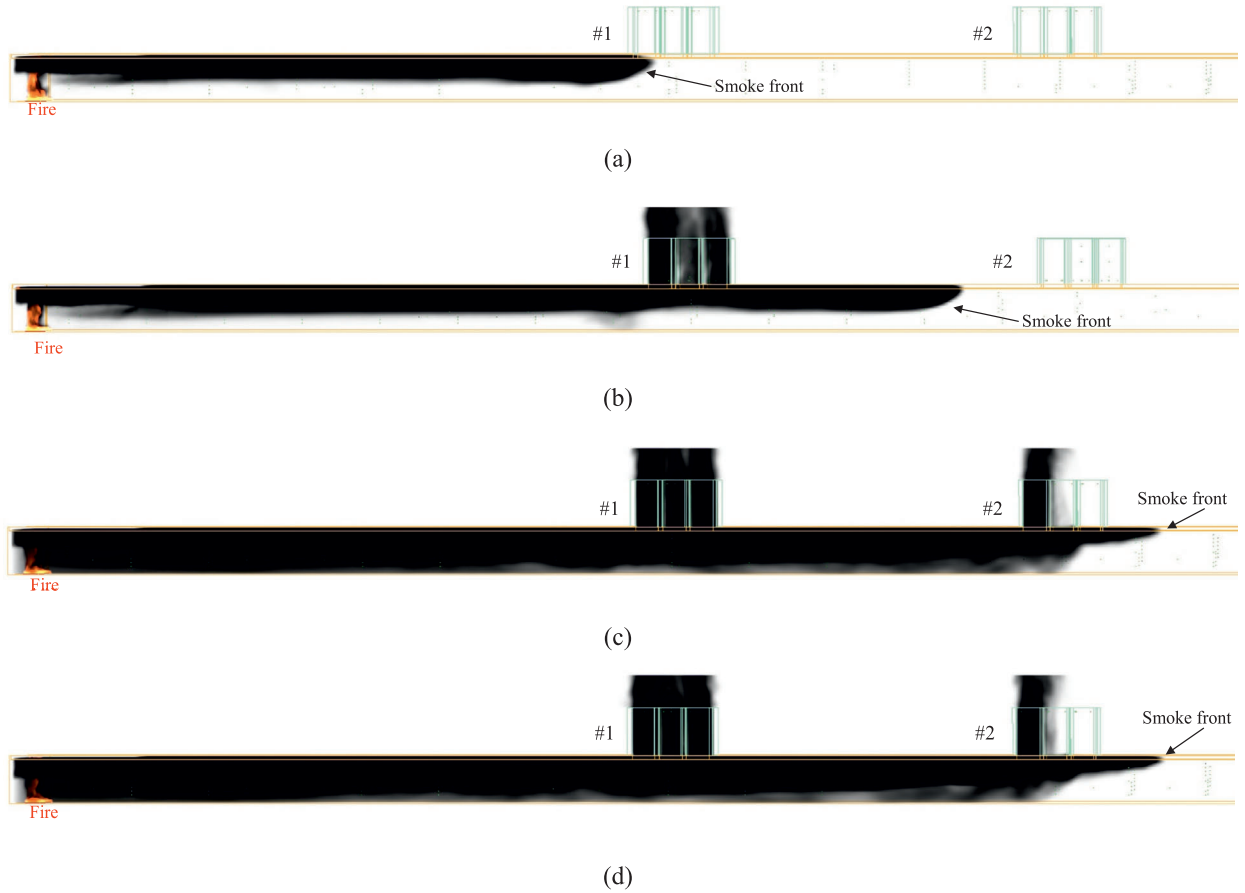

Fig. 9. Smoke views at different times in case 8 ($s_{\text{f-us1}} = 80$ m, $Q = 20$ MW). (a) $t = 50$ s, (b) $t = 100$ s, (c) $t = 300$ s, and (d) $t = 500$ s.

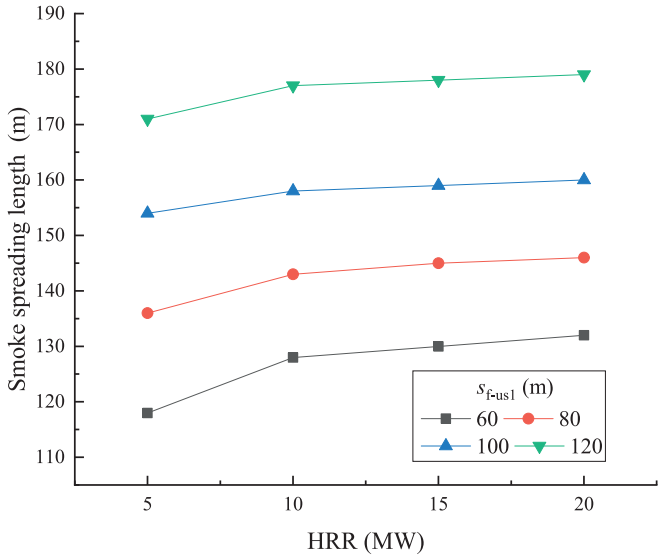

Fig. 10. Smoke spreading lengths after 400 s under stable state in all cases.

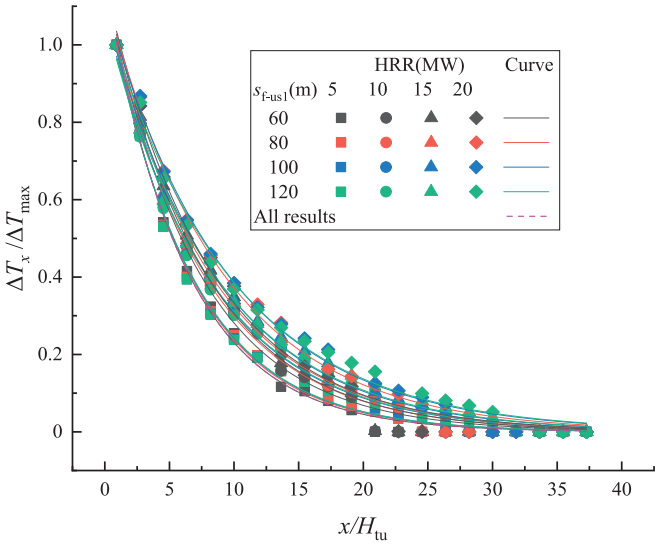

Fig. 12. Dimensionless smoke ceiling temperatures away from the fire source and their fitting curves.

smoke accumulates beneath the ceiling, driven by buoyancy, and then moves towards the right entrance. Shaft #1 always plays an important role in exhausting after the smoke arrives at it. A steady state nearly remains after 400 s, and the smoke front basically stays under the bottom of shaft #2, which has a weak exhausting ability. Based on the smoke views, the steady smoke fronts in all cases are determined and depicted in Fig. 10. It is known that the lengths of the smoke fronts increase evidently with the spacing of $s_{f\text{-}us1}$; they also increase with HRRs, but the tendencies slow down. The smoke fronts are 130 m away from the fire sources under the 60 m spacing $s_{f\text{-}us1}$, 140 m under the 80 m spacing, 160 m under the 100 m spacing, and 180 m under the 120 m spacing, and they are all about under the bottom of shaft #2.

Regarding ceiling smoke temperature, Fig. 11 shows its contours in the range of 0 to 200 m away from the fire source at $t = 500$ s under steady state in case 8 ($s_{f\text{-}us1} = 80$ m, HRR = 20 MW). It can be observed that in the driving zone within a range of 130 m from the fire source, the temperature of the upper space is higher, indicating the presence of the smoke layer. The temperature of the lower space is lower, indicating the air layer. The stratification between the smoke and the air is clear (Luan et al., 2025). Furthermore, shaft #1 is filled with hot smoke. Beyond 130 m from the fire source, the temperatures both in the driving zone and inside shafts #2 and #3 return to ambient levels. This indicates that the hot smoke has not reached these areas. These observations are consistent with the smoke distributions shown in Fig. 8.

Taking the maximum ceiling temperature above the fire source as the reference temperature T_{max} (K), the ceiling temperature T_x (K) at the distance x from the fire source, then the dimensionless spreading distances x/H_{tu} and the dimensionless ceiling smoke temperatures $(T_x - T_a)/(T_{max} - T_a)$ are determined. These scatters are plotted in Fig. 12 under all cases. After observing them, the relationships are determined to be a kind of exponential decay function for any one case or all cases combined, as seen in Eq. (12):

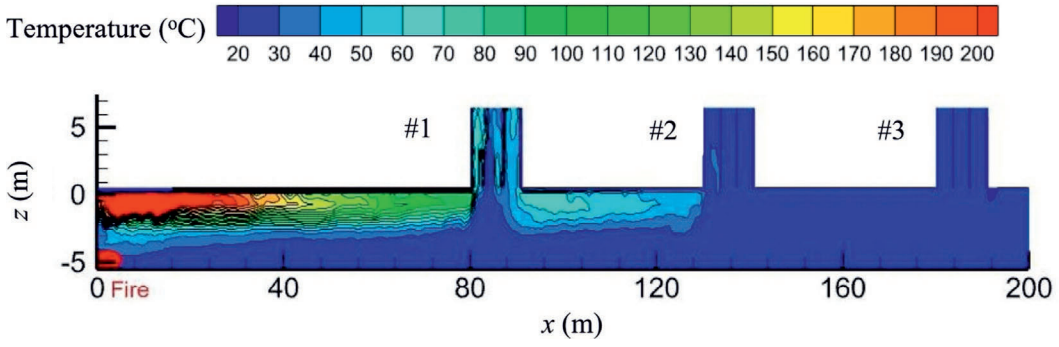

Fig. 11. Ceiling temperature contours in the range of 0 to 200 m in longitude at $t = 500$ s in case 8.

Table 4
Fitting parameters in Eqs. (12) and (13), and the correlation coefficients R^2.

Case No.	Eq. (12)			Eq. (13)			
	a_1	b_1	R^2	a_2	b_2	c_2	R^2
1–4	1.16/1.15/1.16/1.16	0.16/0.14/0.13/0.12	>0.98	2.33	0.54	−0.39	>0.97
5–8	1.15/1.12/1.12/1.13	0.16/0.13/0.12/0.11	>0.98	2.59	0.69	−0.45	>0.97
9–12	1.14/1.08/1.09/1.11	0.16/0.13/0.12/0.11	>0.98	2.95	0.80	−0.59	>0.98
13–16	1.14/1.08/1.07/1.08	0.15/0.12/0.11/0.10	>0.98	3.39	0.97	−0.65	>0.97
All results	1.15	0.16	0.98	–	–	–	>0.90

$$\frac{\Delta T_x}{\Delta T_{\max}} = \frac{T_x - T_a}{T_{\max} - T_a} = a_1 e^{-b_1(x/H_{tu})}, \quad (12)$$

where a_1 is the temperature empirical coefficient, and b_1 is the temperature attenuation coefficient. The larger the b_1, the faster the decay. The fitted curves are depicted in Fig. 12. Values of a_1, b_1, and the correlation coefficient R^2 are listed in Table 4. It is known that values of a_1 are in the range of 1.07 to 1.16, which are all about 1.10. Values of b_1 are in the range of 0.10 to 0.16 and decrease with the increase of $s_{f\text{-}us1}$ under the same HRR when comparisons among cases 1, 5, 9, 13, cases 2, 6, 10, 14, cases 3, 7, 10, 14, cases 4, 8, 11, 15, or cases 5, 9, 12, 16. It can be explained that the larger spacing $s_{f\text{-}us1}$ contributes to less heat loss to the outside. When comparing cases 1 to 4, 5 to 8, 9 to 12, or 13 to 16 under the same $s_{f\text{-}us1}$, the larger the HRR, the smaller the b_1, revealing the evident influence of HRR on the temperature decay. All values of R^2 are larger than 0.98, indicating a good agreement with the exponential decay expression.

6.2 Smoke exhaust or backflow for shafts and entrances

Figure 13 presents the velocity contours and their streamlines of the whole tunnel at t = 500 s in case 8 ($s_{f\text{-}us1}$ = 80 m, HRR = 20 MW). It can be seen that, in the driving zone, the smoke under the ceiling spreads longitudinally towards the right entrance in the region of the fire source and shaft #2-1, but the reversal flows exist widely in other areas. Among the shafts, only unit shafts #1-1 to #3 and #2-1 exhibit exhaust behavior with velocities reaching up to 3.0 m/s, whereas the others display reversal flows. Most of the inhaled air exhibits strong momentum, impinging directly onto the ground. For example, the inflow velocity reaches up to −1.5 m/s in unit shaft #2-2. All these reversal flows occupy a large area of the whole tunnel, showing a strong suction effect, which is driven by the negative pressures generated around the fire source due to combustion. It is noteworthy that for the shafts experiencing backflow, the non-dimensional

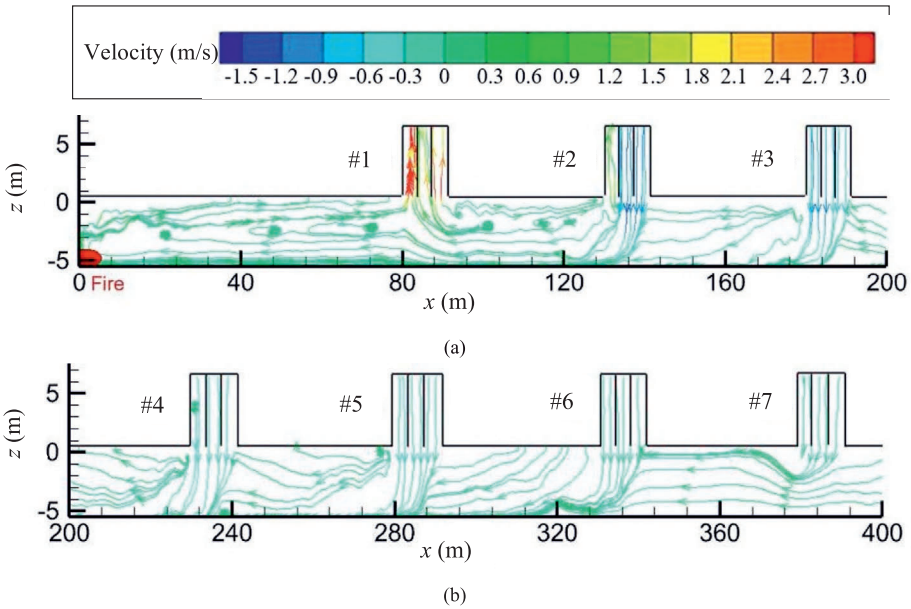

Fig. 13. Velocity contours and their streamlines of the whole tunnel at t = 500 s in case 8. (a) 0–200 m away from the fire source, and (b) 200–400 m away from the fire source.

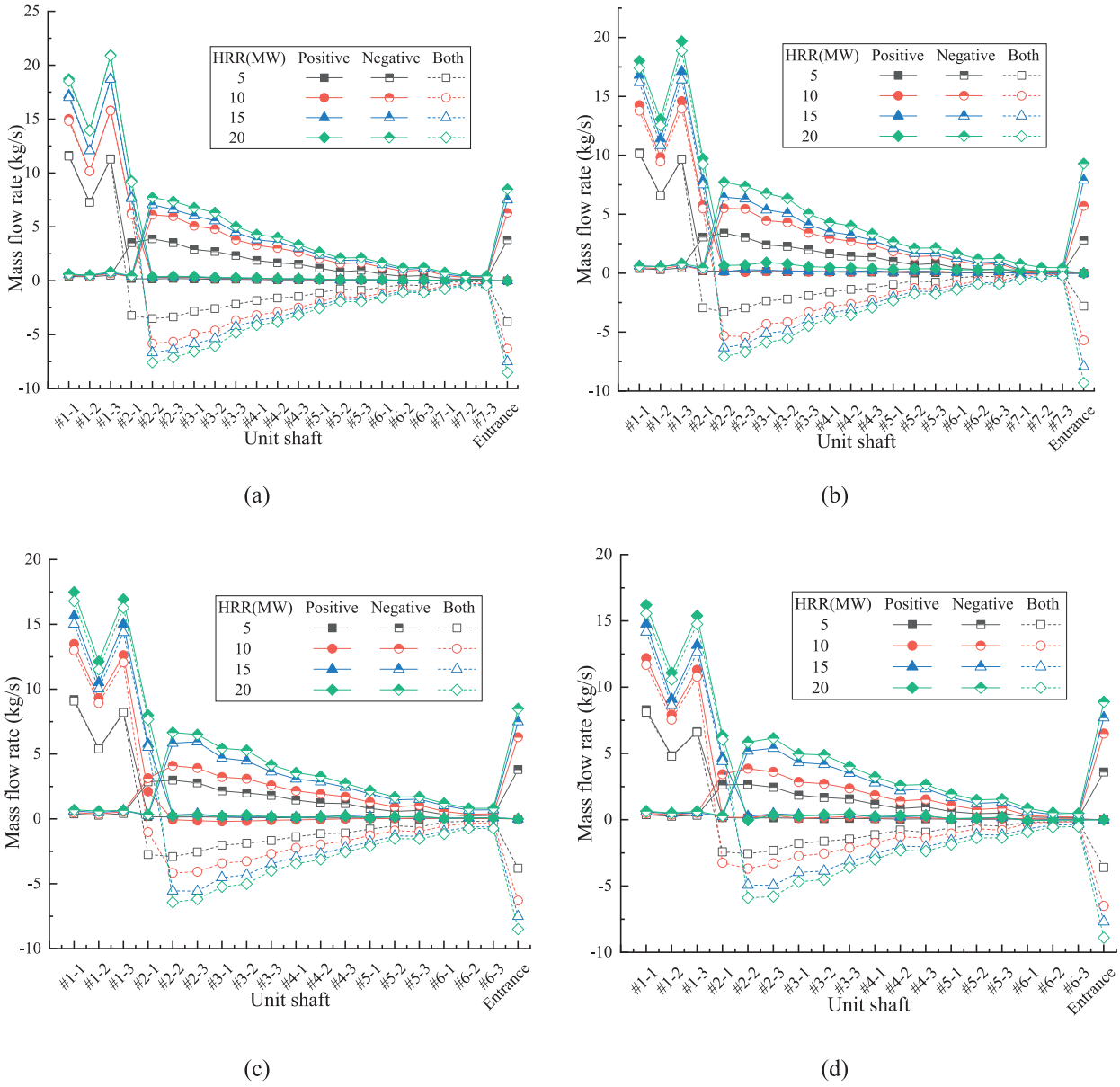

Fig. 14. Mass flow rates of all unit shafts and the right entrance in three directions under all cases. (a) $s_{\text{f-us1}} = 60$ m, (b) $s_{\text{f-us1}} = 80$ m, (c) $s_{\text{f-us1}} = 100$ m, and (d) $s_{\text{f-us1}} = 120$ m.

number *Ri'* is meaningless because the vertical buoyancy forces are so small to be neglected. Additionally, the horizontal inertia forces contributing to these reversal flows are directed towards the fire source.

Figure 14 presents the mass flow rates of all unit shafts and the right entrance at $t = 500$ s under all cases, which are monitored, respectively, in three directions of positive, negative, and both. As far as the positive flow rate, unit shafts #1-1, #1-2, #1-3, and #2-1 always own it, reaching up to 21.5 kg/s due to its proximity to the fire source, followed by a stronger thermal buoyancy. In total, the larger the $s_{\text{f-us1}}$ or the farther away from the fire source, the lower the positive rate. There is an exception that unit shaft #1-3 has some larger values than unit shafts #1-1 and #2. Regarding the negative flow rate, all unit shafts of shafts #2 to #7 and the right entrance own it, reaching up to 7.5 s and 9.0 kg/s, respectively. The larger the $s_{\text{f-us1}}$ or the farther away from the fire source, the lower the negative rate. Finally, the net mass flow rates in both directions are exactly the rate difference between the positive and the negative. Its values are larger than zero for shaft #1, showing an exhaust ability, and smaller than zero for other shafts, showing an inhale ability. However, there is a note that a bidirectional flow exists in unit shaft #2-1 under most cases, and the net mass flow rate can be larger or smaller than zero.

Furthermore, the net mass flow rates are summarized on all exhaust shafts, all backflow shafts, the entrance at $t = 500$ s under all cases, and their results are depicted in Fig. 15. It is known that, in any case, the total exhaust rate

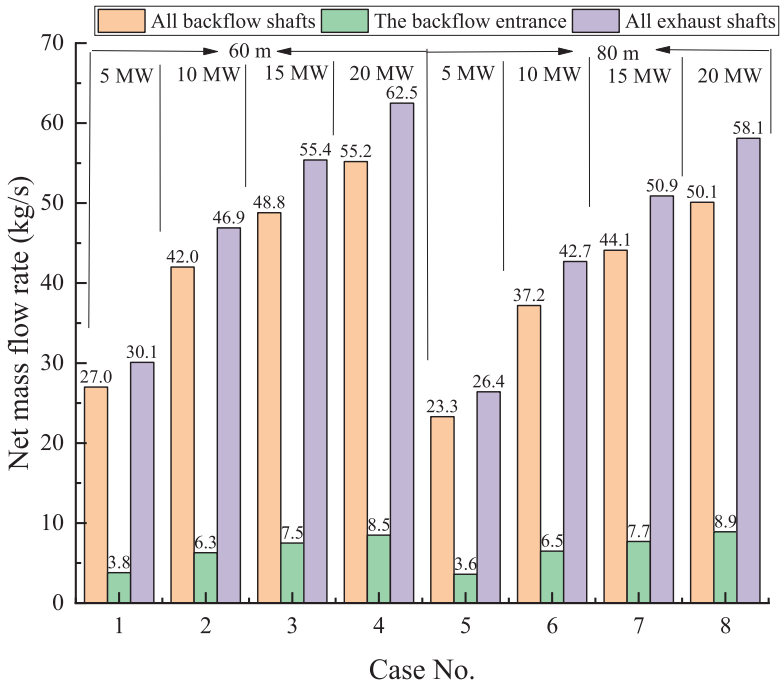

(a)

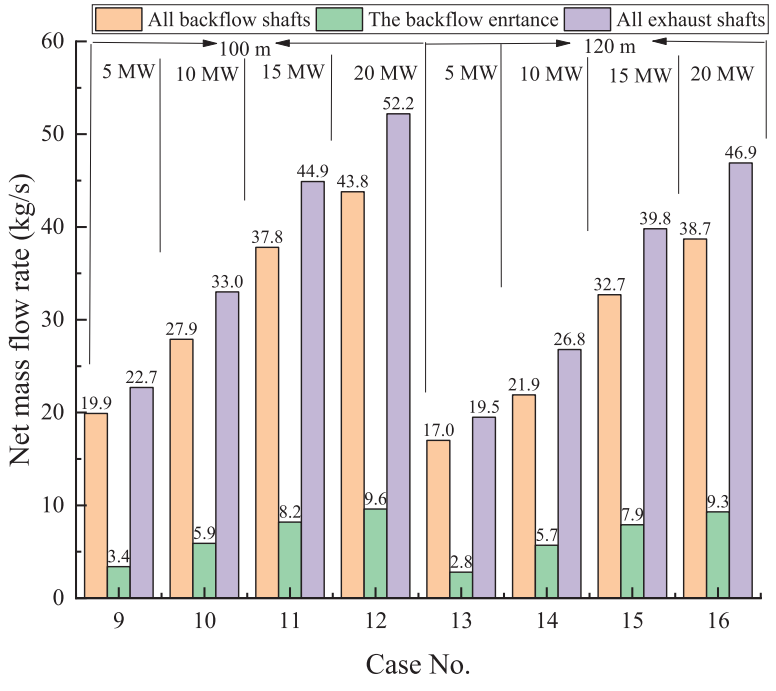

(b)

Fig. 15. Net mass flow rates of all shafts and the right entrance at $t = 500$ s under all cases. (a) Cases 1–8, and (b) cases 9–16.

remains nearly identical to the total backflow rate, confirming mass conservation. The net flow rates differ in cases that are in the range of 26.4 to 62.5 kg/s for all exhaust shafts, 23.3 to 55.2 kg/s for all backflow shafts, and 3.8 to 8.9 kg/s at the right entrance. Under any spacing $s_{\text{f-us1}}$, the net flow rates in the exhaust or backflow increase with the increase of HRR, and it is because that a larger HRR would generate a larger amount of smoke, contributing to a larger supply of air. Under any HRR, the net flow rates in all exhaust or backflow decrease with the increase

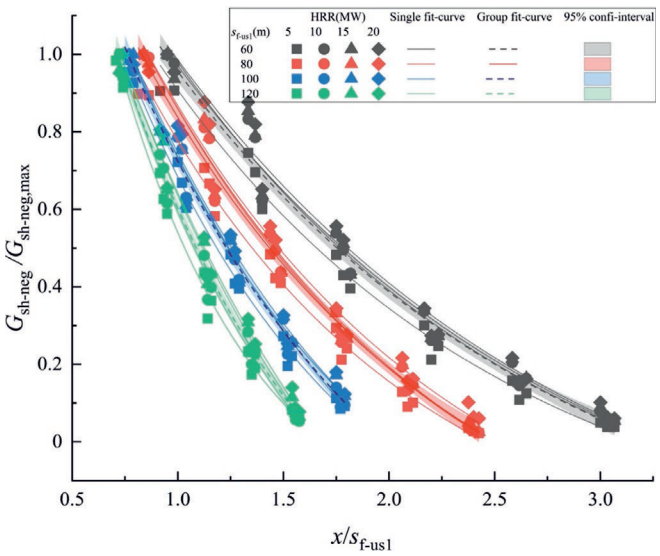

Fig. 16. Mass flow rates of all unit shafts in negative under all cases and their fitting curves.

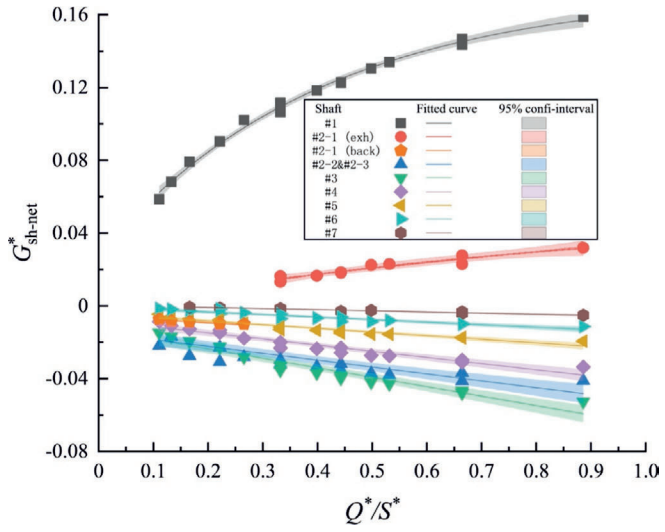

Fig. 17. Relationships of $G^*_{sh\text{-}net}$ against Q^*/S^* and its fitting curves under all cases.

of spacing $s_{f\text{-}us1}$, and it can be explained that the increased spacing generates a decreased opening area ratio k, then the outside air has more difficulty in entering the tunnel. Regarding the backflow, there is a note that, in all cases, the net flow rate at the right entrance is evidently smaller than that of the shafts, also nearly unaffected by the spacing $s_{f\text{-}us1}$, due to its being farthest away from the fire source.

6.3 Fitted mass flow rates of shafts

The negative mass flow rate of one unit shaft is taken as $G_{sh\text{-}neg}$ (kg/s), the maximum negative mass flow rate among all unit shafts as $G_{sh\text{-}neg,max}$, and the distance of one unit shaft away from the fire source as x (m). For any unit shaft under all cases, the dimensionless distance $x/s_{f\text{-}us1}$ and the dimensionless negative mass flow rate $G_{sh\text{-}neg}/G_{sh\text{-}neg,max}$ can be determined, and the relationships are plotted in Fig. 16. A kind of exponential decay function is established, as seen in Eq. (13):

$$\frac{G_{sh\text{-}neg}}{G_{sh\text{-}neg,max}} = a_2 e^{-b_2(x/s_{f\text{-}us1})} + c_2, \tag{13}$$

where both a_2 and c_2 are the empirical coefficients and b_2 is the decay coefficient. The larger the b_2, the faster the decay. The fitted curves under each case and four group cases of 1 to 4 ($s_{f\text{-}us1}$ = 60 m), 5 to 8 ($s_{f\text{-}us1}$ = 80 m), 9 to 12 ($s_{f\text{-}us1}$ = 100 m), and 13 to 16 ($s_{f\text{-}us1}$ = 120 m) are depicted in Fig. 16. Values of a_2, b_2, c_2, and the correlation coefficients R^2 under four group cases are listed in Table 5. It is known that values of b_2 are in the range of 0.54 to 0.97. All values of R^2 are larger than 0.98, indicating a good agreement with the exponential decay expression. The HRR has little influence on the $G_{sh\text{-}neg}/G_{sh\text{-}neg,max}$ under any spacing $s_{f\text{-}us1}$. However, when comparing group cases of 1 to 4, 5 to 8, 9 to 12, and 13 to 16, the larger the $s_{f\text{-}us1}$, the larger the b_2, showing a faster decay.

For all shafts under all cases, values of the Q^*/S^* and the dimensionless net mass flow rates $G^*_{sh\text{-}net}$ are determined based on Eq. (11). The results are presented as scatter points in Fig. 17. There is an exception for shaft #2: unit shaft #2-1 exhibits either exhaust or backflow behavior under cases, and its corresponding $G^*_{sh\text{-}net}$ is calculated separately for each behavior mode. In contrast, unit shafts #2-2 and #3 consistently exhibit backflow, so their flow rates are cumulatively summed. Furthermore, relationships

Table 5
Fitting parameters of all shafts in Eq. (14) and the correlation coefficients R^2.

Parameters	Exhaust shaft		Backflow shaft						
	#1	#2-1	#2-1	#2-2 and #2-3	#3	#4	#5	#6	#7
a_3	0.03	0.007	–	–	–	–	–	–	–
b_3	0.14	0.053	–	–	–	–	–	–	–
c_3	2.48	1.09	–	–	–	–	–	–	–
a_4	–	–	−0.005	−0.014	−0.013	−0.008	−0.004	−0.005	−0.004
b_4	–	–	0.016	0.037	0.052	0.034	0.021	0.013	0.006
R^2	0.92	0.91	0.91	0.82	0.92	0.91	0.91	0.89	0.94

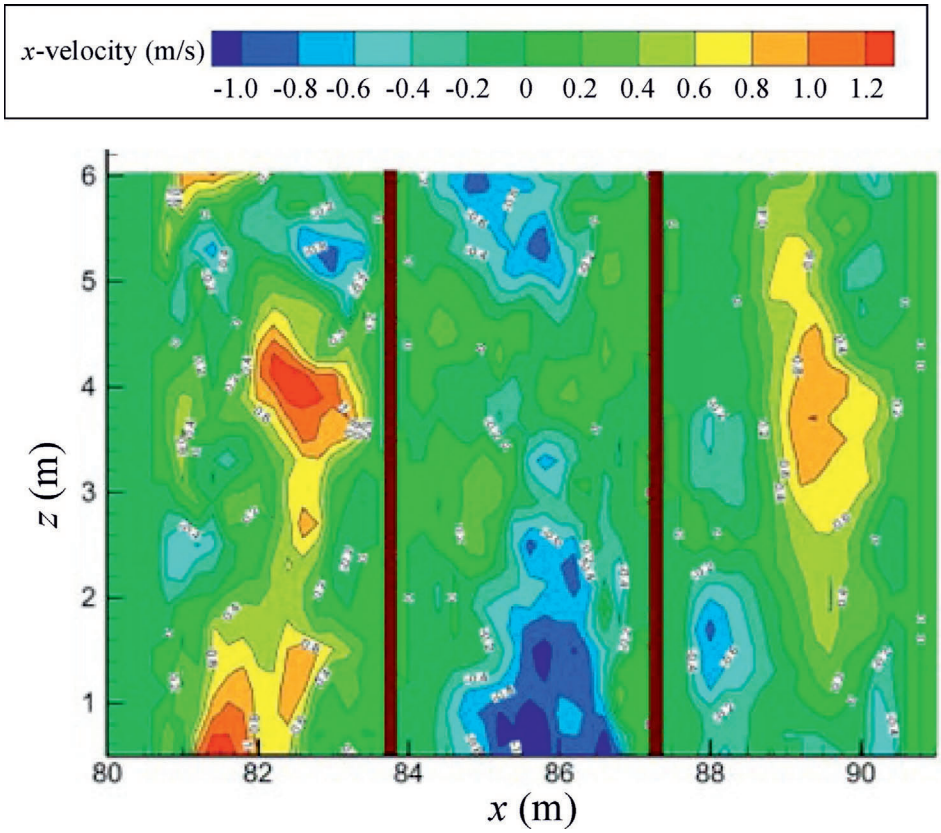

Fig. 18. Velocity contours in x-direction on the plane of $y = 1.5$ m inside shaft #1 at $t = 500$ s in case 8.

between the $G^*_{\text{sh-net}}$ and the Q^*/S^* are determined to be kinds of power-exponential function for the exhaust shafts, and linear function for the backflow shafts, respectively. Equation (14) gives the following result:

$$G^*_{\text{sh-net}} = \begin{cases} a_3 + b_3\left(1 - e^{-c_3(Q^*/S^*)}\right) & \text{Exhaust shafts (\#1 – \#2)}, \\ a_4 - b_4(Q^*/S^*) & \text{Backflow shafts (\#2 – \#7)}, \end{cases} \tag{14}$$

where parameters of a_3, b_3, and a_4 are all empirical coefficients; c_3 is the growth coefficient; b_4 is the decay coefficient. The larger the c_3, the faster the growth. The larger the absolute value of b_4, the faster the decay. The fitted curves are depicted in Fig. 17. Values of all parameters and the correlation coefficients R^2 are listed in Table 5. Regarding the exhaust shafts, values of $G^*_{\text{sh-net}}$ are in the range of 0.05 to 0.16, which increase with the increase of Q^*/S^*. The coefficient c_3 is 2.48 for shaft #1 and 1.09 for unit shaft #2-1, indicating a slower growth. Regarding backflow shafts, values of $G^*_{\text{sh-net}}$ are in the range of −0.06 to 0, which decrease with the increase of Q^*/S^*. Values of b_4 range from 0.006 to 0.052, and shaft #3 owns the largest value, indicating a fastest decay, whereas shaft #7 owns the slowest decay.

6.4 Positions of the neutral plane inside shafts

As an example of case 8, Fig. 18 depicts the velocity contours in the x-direction on the plane of $y = 1.5$ m inside shaft #1 at 500 s under a stable state. It is known that complex flows exist inside all three unit shafts and differ among them. The x-velocity can reach up to about 1.0 m/s in unit shaft #1-1, −1.0 m/s in unit shaft #1-2, and 0.8 m/s in unit shaft #1-3. In the same unit shaft, there are larger values in the middle of all unit shafts, and smaller ones near the sidewalls. It is easily known that the flows are restricted by the solid walls to some extent.

After averaging three x-velocities at each monitored height of each unit shaft at 500 s, the horizontal x-velocities in height are obtained. Observing its distributions and determining the zero value, the NPH is determined. As an example of shafts #1, #2, and #5 in case 8, Fig. 19 gives these results. It is known that the x-velocities change largely in height, which is in the range of −0.35 to 0.5 m/s in shaft #1, −0.12 to 0.12 m/s in shaft #2, and −0.03 to 0.04 m/s in shaft #5. In general, the farther the shaft is from the fire source, the smaller the x-velocity due to the weaker thermal buoyancy. Values of NPH have small differences among unit shafts in one shaft but differ evidently among shafts. They are in the range of 2.1 to 3.1 m in shaft #1, 3.85 to 4.0 m in shaft #2, and 4.2 to 4.8 m in shaft #5. The farther away from the fire source, the higher the NPH.

Figure 20 presents the relationships between the shaft NPH and the shaft net mass flow rate $G_{\text{sh-net}}$ (discussed in Section 6.2) under all cases. It can be found that values of the NPH range from 1.4 m to 5.4 m, and the exhaust shafts own it in the range of 1.4 m to 3.6 m, whereas the

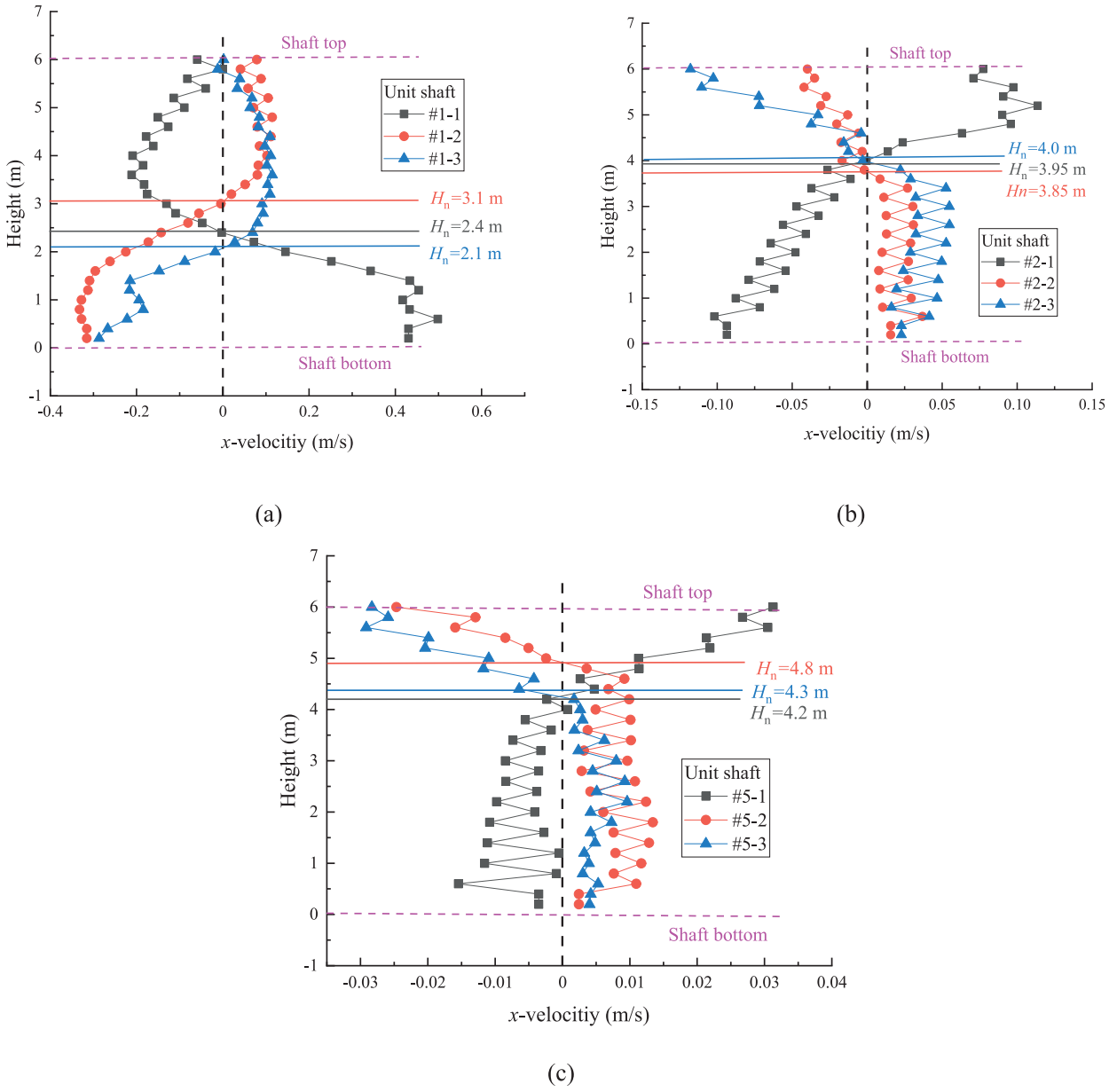

Fig. 19. Horizontal velocities in height inside shafts and determinations of neutral plane position in case 8. (a) Shaft #1, (b) shaft #2, and (c) shaft #5.

backflow shafts own larger values in the range of 3.2 m to 5.4 m. For any $s_{\text{f-us1}}$, especially 60 m, a smaller HRR results in a smaller absolute value of the $G_{\text{sh-net}}$, followed by a higher NPH. It can be easily understood that a weak thermal buoyancy, which originates from a small fire power, is not conducive to the shaft's exhaust ability. Furthermore, the shaft NPHs decrease with the increase of the absolute values of the $G_{\text{sh-net}}$. A correlation is fitted linearly between them, as seen in Eq. (15):

$$H_{\text{n}} = a_5 - b_5|G_{\text{sh - net}}|, \tag{15}$$

where a_5 is the empirical value, m; b_5 is the decrease coefficient, m/(kg/s). Values of b_5 are around 8.0 for the exhaust shafts, which are to be 7.34 ($s_{\text{f-us1}}$ = 60 m), 8.05 ($s_{\text{f-us1}}$ = 80 m), 8.21 ($s_{\text{f-us1}}$ = 100 m), and 8.42 ($s_{\text{f-us1}}$ = 120 m), respectively. The R^2 corresponds to 0.91, 0.97, 0.98, and 0.97, showing good correlations. Values of b_5 are around 4.0 for the backflow shafts, which are to be 3.37 ($s_{\text{f-us1}}$ = 60 m), 4.65 ($s_{\text{f-us1}}$ = 80 m), 4.82 ($s_{\text{f-us1}}$ = 100 m), and 4.78 ($s_{\text{f-us1}}$ = 120 m), respectively. The R^2 corresponds to 0.81, 0.95, 0.97, and 0.98, showing good correlations. Furthermore, b_5 increases with the increase of $s_{\text{f-us1}}$, indicating a faster decrease of the NPH. The reason is that the longer the smoke arrives at the first shaft, the more the hot smoke accumulates, then the stronger the shaft's exhaust ability, leading to a lower NPH.

7 Conclusions

A tunnel with the dimension of 400 m (length) × 12 m (width) × 5.5 m (height) is established using FDS software, and a number of 6–7 shafts are arranged over the ceiling

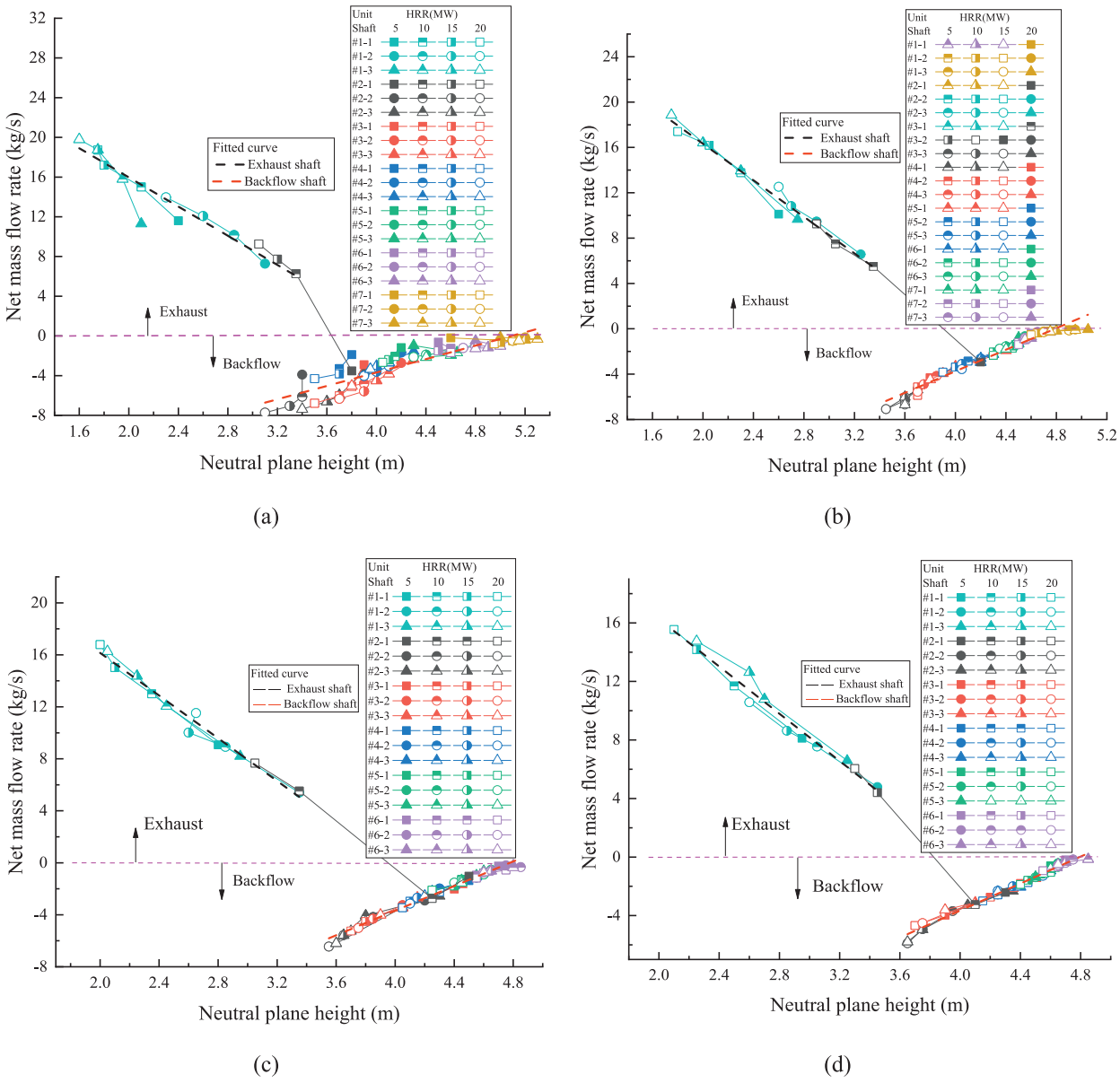

Fig. 20. Relationships between neutral plane heights and net mass flow rates under all cases. (a) $s_{\text{f-us1}} = 60$ m, (b) $s_{\text{f-us1}} = 80$ m, (c) $s_{\text{f-us1}} = 100$ m, and (d) $s_{\text{f-us1}} = 120$ m.

with each having a size of 9.0 m (length) × 3.0 m (width) × 6.0 m (height). A mirror vent is adopted on the left entrance. After being verified by both the 1/16 small-scale experiment and one full-scale experiment, a series of numerical simulations are carried out to investigate the spread of fire smoke, especially the shaft backflow phenomenon. Influencing factors include four HRRs of 5, 10, 15, and 20 MW and four spacings $s_{\text{f-us1}}$ of 60, 80, 100, and 120 m.

The conclusions drawn are the following:

(1) The smoke spreading length under the ceiling is almost not affected by HRR, but increases with the increase of $s_{\text{f-us1}}$. A power exponential function provides a good fit for the dimensionless ceiling smoke temperature $(T_x - T_a)/(T_{\max} - T_a)$ away from the fire source. Values of the decay coefficient b_1 range from 0.10 to 0.16 and decrease only with the increase of HRR.

(2) The dimensionless shaft negative mass flow rate $G_{\text{sh-neg}}/G_{\text{sh-neg,max}}$ follows a good power exponential rule away from the fire source. The decay coefficient b_2 increases only with the increase of $s_{\text{f-us1}}$. The dimensionless shaft net mass flow rate $G^*_{\text{sh-net}}$ follows a good power exponential relationship with Q^*/S^* for the exhaust shafts and a good linear relationship for the backflow shafts.

(3) Only the shaft closest to the fire source consistently exhibits the smoke exhaust, while others experience varying degrees of backflow. So, it is critical to design

each shaft with enough size, as the location of a fire source is unpredictable. The shaft NPHs range from 1.4 to 3.6 m for the exhaust shafts and 3.2 to 5.4 m for the backflow shafts. Furthermore, the NPHs decrease linearly with the increase of the absolute values of the shaft net mass flow rate $G_{\text{sh-net}}$. Values of the decrease coefficient b_5 are around 8.0 for the exhaust shafts and 4.0 for the backflow shafts.

These results enhance the understanding of the global smoke behaviors of multiple shafts in URTS, providing valuable data for improving the shaft ventilation design and the fire safety regulations. Future work aims to establish a dimensionless criterion to assess the shaft smoke backflow and investigate the influence of ambient wind.

Data availability

The data that support the findings of this study are available from the corresponding author upon reasonable request.

CRediT authorship contribution statement

Daolong Xiong: Writing – original draft, Methodology, Data curation, Conceptualization. **Shiqi Zhang:** Writing – review & editing, Formal analysis, Data curation. **Yan Ouyang:** Writing – review & editing, Formal analysis, Data curation. **Yan Tong:** Supervision, Project administration, Funding acquisition, Conceptualization. **Zelin Liu:** Validation, Software, Investigation. **Kaiquan Chen:** Formal analysis, Data curation. **Peng Wang:** Software, Data curation. **Yinqing Zhou:** Software, Investigation.

Declaration of competing interest

The authors declare that they have no known competing financial interests or personal relationships that could have appeared to influence the work reported in this paper.

Acknowledgement

This study was supported by the National Natural Science Foundation of China (Grant No. 52278112). We are grateful to the High Performance Computing Center of Nanjing Tech University for providing computational resources.

References

Anghel, I., Octavian, L., Codescu, S., Pesic, D. J., & Constantin, P. (2017). Experimental investigation on the characteristics of fires in a reduced 1/10 scale road tunnel using different combustible liquid pools, Acta Tech. Napocensis-Series. *Applied Mathematics and Mechanics (English Edition), 60*.

Babrauskas, V. (1983). Estimating large pool fire burning rates. *Fire Technology, 19*(4), 251–261.

Bibin, C., Devan, P. K., Senthil Kumar, S., Gopinath, S., Sheeja, R., Kanthavelkumaran, N., Gobinath, S., & Ashok, K. G. (2021). Thermal performance of lithium-Ion battery pack using forced air circulation system. *Materials Today: Proceedings, 46*, 3670–3676.

Cheng, H. H., Liu, C., Chen, J. F., Wu, L., Zhao, Y. T., & Zhong, M. H. (2022). Full-scale experimental study on fire under natural ventilation in the T-shaped and curved tunnel groups. *Tunnelling and Underground Space Technology, 123*, 104442.

Chow, W. K., & Gao, Y. (2011). Buoyancy and inertial force on oscillations of thermal-induced convective flow across a vent. *Building and Environment, 46*(2), 315–323.

Chow, W. K., Gao, Y., Zhao, J. H., Dang, J. F., & Chow, N. C. L. (2016). A study on tilted tunnel fire under natural ventilation. *Fire Safety Journal, 81*, 44–57.

Cong, H. Y., Bi, M. S., Ren, J. J., Li, B., Bi, Y. B., Li, Y. C., Jiang, H. P., & Gao, W. (2020). Experimental studies on the smoke extraction performance by natural ventilation with a board-coupled shaft in a deep buried tunnel. *Tunnelling and Underground Space Technology, 106*, 103613.

Cong, H. Y., Wang, X. S., Zhu, P., Jiang, T. H., & Shi, X. J. (2017). Improvement in smoke extraction efficiency by natural ventilation through a board-coupled shaft during tunnel fires. *Applied Thermal Engineering, 118*, 127–137.

Ding, Y. M., Mei, J. X., Li, X., Lu, K. H., & Li, C. H. (2024). A dimensionless model for smoke backflow length prediction with mobile ventilation in tunnel fire. *Thermal Science and Engineering Progress, 56*, 103026.

Fan, C. G., Li, X. Y., Mu, Y., Guo, F. Y., & Ji, J. (2017). Smoke movement characteristics under stack effect in a mine laneway fire. *Applied Thermal Engineering, 110*, 70–79.

Gao, Z. H., Li, L. J., Sun, C. P., Zhong, W., & Yan, C. B. (2022). Effect of longitudinal slope on the smoke propagation and ceiling temperature characterization in sloping tunnel fires under natural ventilation. *Tunnelling and Underground Space Technology, 123*, 104396.

Gao, Z. H., Li, L. J., Zhong, W., & Liu, X. (2021). Characterization and prediction of ceiling temperature propagation of thermal plume in confined environment of common services tunnel. *Tunnelling and Underground Space Technology, 110*, 103714.

Gong, L., Jiang, L., Li, S. Y., Shen, N., Zhang, Y. C., & Sun, J. H. (2016). Theoretical and experimental study on longitudinal smoke temperature distribution in tunnel fires. *International Journal of Thermal Sciences, 102*, 319–328.

Guo, Q. H., Li, Y. Z., Ingason, H., Yan, Z. G., & Zhu, H. H. (2021). Theoretical and numerical study on mass flow rates of smoke exhausted from short vertical shafts in naturally ventilated urban road tunnel fires. *Tunnelling and Underground Space Technology, 111*, 103782.

Guo, Q. H., Zhu, H. H., Zhang, Y. X., Shen, Y., Zhang, Y. P., & Yan, Z. G. (2020). Smoke flow in full-scale urban road tunnel fires with large cross-sectional vertical shafts. *Tunnelling and Underground Space Technology, 104*, 103536.

He, K., Cheng, X., Li, Y. Z., Ingason, H., Shi, Z., Yang, H., & Zhang, H. (2021). Experimental study on flame characteristics of double fires in a naturally ventilated tunnel: Flame merging, flame tilt angle and flame height. *Tunnelling and Underground Space Technology, 114*, 103912.

Hu, L. H., Huo, R., Li, Y. Z., Wang, H. B., & Chow, W. K. (2005). Full-scale burning tests on studying smoke temperature and velocity along a corridor. *Tunnelling and Underground Space Technology, 20*(3), 223–229.

Hu, L. H., Tang, F., Yang, D., Liu, S., & Huo, R. (2010). Longitudinal distributions of CO concentration and difference with temperature field in a tunnel fire smoke flow. *International Journal of Heat and Mass Transfer, 53*(13–14), 2844–2855.

Ingason, H. (1995). Design fires in tunnels. In *Proceedings of Asia flame 95: The International Conference on Fire Science and Engineering* (77–86). September, 1995, Hangzhou, China.

Ji, J., Gao, Z. H., Fan, C. G., & Sun, J. H. (2013a). Large Eddy simulation of stack effect on natural smoke exhausting effect in urban road tunnel fires. *International Journal of Heat and Mass Transfer, 66*, 531–542.

Ji, J., Gao, Z. H., Fan, C. G., Zhong, W., & Sun, J. H. (2012). A study of the effect of plug-holing and boundary layer separation on natural ventilation with vertical shaft in urban road tunnel fires. *International Journal of Heat and Mass Transfer, 55*(21–22), 6032–6041.

Ji, J., Han, J. Y., Fan, C. G., Gao, Z. H., & Sun, J. H. (2013b). Influence of cross-sectional area and aspect ratio of shaft on natural ventilation in urban road tunnel. *International Journal of Heat and Mass Transfer, 67*, 420–431.

Jiao, A., Zeng, W., Fan, C., Bu, R., Chen, H., Chen, Y., Xie, B., & Li, Y. (2025). Experimental study on multiple fire hazards both inside and outside a naturally ventilated tunnel: Burning rate and flame characteristics of unequal fires. *Tunnelling and Underground Space Technology, 158*, 106442.

Karlsson, B., & Quintiere, J. G. (2000). *Enclosure fire dynamics*. CRC Press.

Li, L. J., Ji, J., Fan, C. G., Sun, J. H., Yuan, X. Y., & Shi, W. X. (2014). Experimental investigation on the characteristics of buoyant plume movement in a stairwell with multiple openings. *Energy and Buildings, 68*, 108–120.

Li, Y. Z., & Ingason, H. (2018). Overview of research on fire safety in underground road and railway tunnels. *Tunnelling and Underground Space Technology, 81*, 568–589.

Liang, W. K., Wang, Y., Wen, Z. H., Hao, M., Zhou, R., & Jiang, J. C. (2025). Influence of lateral ambient wind speed on fire smoke behavior in tunnel with unpowered ventilation caps shaft. *Case Studies in Thermal Engineering, 66*, 105776.

Liu, W., Deng, L., Li, H. R., Li, X. C., Shi, C. L., Meng, N., & Tang, F. (2023). Experimental study and machine learning on the maximum temperature beneath tunnel ceiling induced by adjacent tandem fires in longitudinally ventilated tunnel. *International Journal of Thermal Sciences, 187*, 108169.

Luan, D., Chu, T., Bielawski, J., Fan, C., Węgrzyński, W., & Huang, X. (2025). Smoke movement and stratification of tunnel fires under coupled effects of rainfall and ventilation. *Fire Safety Journal, 152*, 104323.

Mao, S. H., & Yang, D. (2016). One-dimensional analysis for optimizing smoke venting in tunnels by combining roof vents and longitudinal ventilation. *Applied Thermal Engineering, 108*, 1288–1297.

McGrattan, K., Hostikka, S., McDermott, R., Floyd, J., Weinschenk, C., & Overholt, K. (2014). *Fire dynamics simulator user's guide*. NIST Special Publication.

Qiu, P. Y., Long, Z., Liu, C., Yang, Y. X., Tian, X. L., & Zhong, M. H. (2021). Full-scale experiment on smoke propagation in metro station tunnel fire under opening the platform screen doors. *Tunnelling and Underground Space Technology, 107*, 103662.

Shao, Z. Y., Li, Y., Cui, H. H., Yu, B. S., & Cong, H. Y. (2024). Numerical investigation of longitudinal location and heat release rate of fire source on neutral plane height and induced flow in longitudinal sloping tunnel fires under natural ventilation. *International Journal of Thermal Sciences, 200*, 108981.

Shi, C. L., Li, J., & Xu, X. (2021). Full-scale tests on smoke temperature distribution in long-large subway tunnels with longitudinal mechanical ventilation. *Tunnelling and Underground Space Technology, 109*, 103784.

Soundararajan, G., Bibin, C., Kumar, A., Devarajan, Y., & Mishra, R. (2025). Synergistic effects of graphene quantum dot additives in waste plastic oil blends: Combustion stability and emission reductions analysis. *Results in Engineering, 25*, 104130.

Tanaka, F., Majima, S., Kato, M., & Kawabata, N. (2015). Performance validation of a hybrid ventilation strategy comprising longitudinal and point ventilation by a fire experiment using a model-scale tunnel. *Fire Safety Journal, 71*, 287–298.

Tanaka, F., Yoshida, K., Ueda, K., & Ji, J. (2021). A simple model for predicting the smoke spread length during a fire in a shallow urban road tunnel with roof openings under natural ventilation. *Fire Safety Journal, 120*, 103106.

Tong, Y., Wang, X., Zhai, J., Niu, X. F., & Liu, L. L. (2014). Theoretical predictions and field measurements for potential natural ventilation in urban vehicular tunnels with roof openings. *Building and Environment, 82*, 450–458.

Wang, Z., Deng, W. H., Zhou, M., Fang, Z., Guan, Y. X., & Tang, Z. (2023). Evaluation of fire smoke and heat exhaust performance of shafts by natural venting in tunnels. *Tunnelling and Underground Space Technology, 131*, 104817.

World Road Association. (1999). *Fire and smoke control in road tunnels* (Report No. 05.05.B). February 2, 2026, https://www.piarc.org/en/order-library/3854-en-Fire%20and%20Smoke%20Control%20in%20Road%20Tunnels.

Yan, T., MingHeng, S., YanFeng, G., & JiaPeng, H. (2009). Full-scale experimental study on smoke flow in natural ventilation road tunnel fires with shafts. *Tunnelling and Underground Space Technology, 24*(6), 627–633.

Yang, D., Du, T., Peng, S. N., & Li, B. Z. (2013). A model for analysis of convection induced by stack effect in a shaft with warm airflow expelled from adjacent space. *Energy and Buildings, 62*, 107–115.

Yang, Y. X., Liu, C., Long, Z., Qiu, P. Y., Chen, J. C., & Zhong, M. H. (2020). Full-scale experimental study on fire under vehicle operations in a sloped tunnel. *International Journal of Thermal Sciences, 158*, 106524.

Yao, Y. Z., Li, Y. Z., Ingason, H., & Cheng, X. D. (2019). Numerical study on overall smoke control using naturally ventilated shafts during fires in a road tunnel. *International Journal of Thermal Sciences, 140*, 491–504.

Ying, H. L., Xu, Z. S., Yin, Y. L., & Yu, Z. H. (2025). Experimental study of smoke back-layering length under coordinated ventilation in underground interconnected tunnel. *Tunnelling and Underground Space Technology, 159*, 106464.

Yuan, Y., Lei, J., & Liu, N. (2024). Experimental research on the flow field and flame geometry of free buoyant diffusion flames with low dimensionless heat release rates. *Combustion and Flame, 269*, 113659.

Zhang, G. L., Peng, T., Tong, Y., Gong, Y. F., Chen, Z., Huang, W. H., & Dai, B. L. (2024). Full-scale experiments on the fire smoke extraction from naturally ventilated shafts for shallow-buried urban road tunnels in hot summer. *Tunnelling and Underground Space Technology, 143*, 105441.

Zhang, T. H., Wang, G. Y., Hu, H. H., Huang, Y. D., Zhu, K., & Wu, K. (2021). Study on temperature decay characteristics of fire smoke backflow layer in tunnels with wide-shallow cross-section. *Tunnelling and Underground Space Technology, 112*, 103874.

Zhao, X. Q., Chi, J. W., Luo, H., Zhou, R., Hao, M., & Jiang, J. C. (2024). Effect of unpowered ventilation caps and shaft parameters on fire smoke spread in the natural ventilation tunnel with shafts. *Journal of Building Engineering, 87*, 109086.

Zhong, M. H., Shi, C. L., He, L., Shi, J. H., Liu, C., & Tian, X. L. (2016). Smoke development in full-scale sloped long and large curved tunnel fires under natural ventilation. *Applied Thermal Engineering, 108*, 857–865.

Zhou, Y. Q., Tong, Z. P., Tong, Y., Xiong, D. L., Liu, Z. L., Chen, K. Q., Zhang, G. L., & Gong, Y. F. (2025). Full-scale experiments on fire smoke spreading respectively under natural and hybrid ventilation in a real urban road tunnel with shafts. *Applied Thermal Engineering, 260*, 124865.

Zhu, B., Cong, H. Y., Shao, Z. Y., Hu, H. R., Ye, L. L., Bi, Y. B., & Zeng, Y. P. (2025). Numerical studies on the synergistic effects of smoke extraction and control performance by mechanical ventilation shafts during tunnel fires. *Underground Space, 21*, 44–64.